Faraday Discussions

Accepted Manuscript

ROYAL SOCIETY OF CHEMISTRY

www.rsc.org/faraday_d

Temperature-induced mobility in Octacalcium Phosphate impacts crystal symmetry:
water dynamics studied by NMR crystallography

Adam Nelson,[1,2] Wassilios Papawassiliou,[3] Subhradip Paul,[3] Sabine Hediger,[3] Ivan Hung,[4] Zhehong Gan,[4] Amrit Venkatesh,[4] W. Trent Franks,[5] Mark E. Smith,[5,6] David Gajan,[7] Gaël De Paëpe,[3] Christian Bonhomme,[1] Danielle Laurencin,[2,*] Christel Gervais[1,*]

[1] LCMCP, UMR 7574, Sorbonne Université, CNRS, Paris, France

[2] ICGM, Univ Montpellier, CNRS, ENSCM, Montpellier, France

[3] IRIG, MEM, Univ. Grenoble Alpes, CEA, CNRS, 38000 Grenoble, France

[4] National High Magnetic Laboratory (NHMFL), Tallahassee, Florida, USA

[5] Department of Physics, University of Warwick, Coventry, CV4 7AL, UK

[6] Department of Chemistry, University of Southampton, SO17 1BJ, UK

[7] CRMN Lyon, UMR 5082 (CNRS, ENS Lyon, Université Lyon 1), Villeurbanne, France

To whom correspondence should be addressed:
christel.gervais_stary@sorbonne-universite.fr
danielle.laurencin@umontpellier.fr

Abstract

Octacalcium phosphate (OCP, $Ca_8(PO_4)_4(HPO_4)_2 \cdot 5H_2O$) is a notable calcium phosphate due to its biocompatibility, making it a widely studied material for bone substitution. It is known to be a precursor of bone mineral, but its role in biomineralisation remains unclear. While the structure of OCP has been the subject of thorough investigations (including using Rietveld refinements of X-ray diffraction data, and NMR crystallography studies), important questions regarding the symmetry and H-bonding network in the material remain. In this study, it is shown that OCP undergoes a lowering of symmetry below 200 K, evidenced by ^1H, ^{17}O, ^{31}P and ^{43}Ca solid state NMR experiments. Using *ab-initio* molecular dynamics (MD) simulations and Gauge Including Projected Augmented Wave (GIPAW) DFT calculations of NMR parameters, the presence of rapid motions of the water molecules in the crystal cell at room temperature is proved. This information leads to an improved description of the OCP structure at both low and ambient temperatures, and helps explain long-standing issues of symmetry. Remaining challenges related to the understanding of the structure of OCP are then discussed.

Faraday Discussions Accepted Manuscript

Introduction

Octacalcium phosphate (OCP, $Ca_8(PO_4)_4(HPO_4)_2\cdot5H_2O$) is a lamellar, hydrated calcium phosphate. It is a direct precursor of hydroxyapatite (HAp).[1] As HAp is the major component of bone mineral, the role of OCP in biomineralisation has been the subject of numerous investigations.[2,3,4,5,6] OCP is a plausible precursor to bone mineral for a number of reasons: it precipitates and further transforms into HAp at physiological pH,[7] and shares striking structural similarities with this phase.[8] Indeed, the lamellar structure of OCP is commonly described as being comprised of an "apatite-like" layer and a "hydrated" interlayer (Fig. 1), which is reminiscent of the hydrated layer found at the surface of bone mineral.[9,10] Yet, although OCP has now been observed *in vivo* in small quantities,[2] its prevalence in the human body and role in biomineralisation are still a matter of debate.
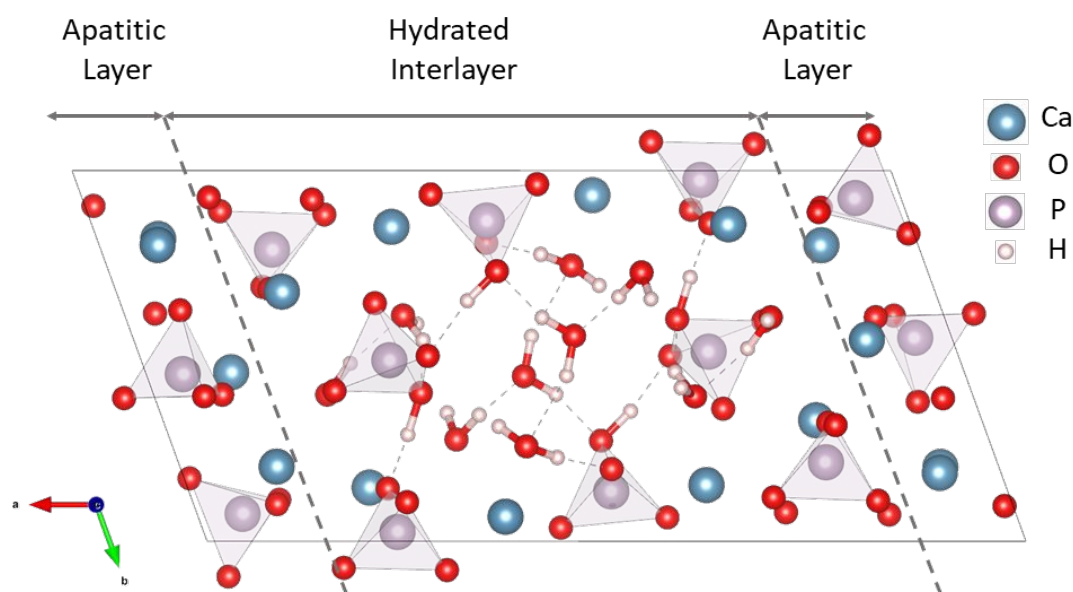

Figure 1: The twinned cell of octacalcium phosphate ($Ca_{16}(PO_4)_8(HPO_4)_4\cdot10H_2O$), divided in two layers, as is commonly described.

Key to OCP's study is an accurate description of its crystal structure. Although the first report of OCP as a distinct calcium phosphate dates back to 1950,[11] determination of its crystal structure was a clear challenge, owing to several unfavourable characteristics. The XRD crystallographic refinements of the phase by Brown *et al.*[1,8,12] faced a number of difficulties. Firstly, synthesising a pure sample of OCP is problematic, as the formation conditions allow its transformation into HAp,[1] and synthesis usually yields a mix of the two phases. The very similar powder X-ray diffraction (pXRD) patterns of OCP and HAp across a wide range of angles means determining the purity of a given synthesis product has been a challenge, until the first high-resolution solid state NMR experiments.[13] The issue of sample purity was addressed by Brown through the study of a single-crystal.[14] Its formation proved extremely difficult, as the synthesis of a sufficiently large crystal, measuring 0.2 mm in length,[12] could not be reproduced by the same team in later studies. Secondly, the large number of atoms (110) in the twinned unit cell, the important and variable number of water molecules clustered in the centre of the twinned cell, and the low symmetry group (*P*-1 or *P*1) mean that Rietveld refinements could only give a limited picture of the structure, particularly concerning the H-bonding network of the interlayer. The most notable issue with the XRD-refined structure of OCP is the lack of a clear symmetry group:

although the apatitic layer exhibits a central symmetry, it is unknown whether this holds true for the interlayer, as apparent disorder limits the accuracy with which the water molecules can be placed in the structure. This, in turn, leaves it with a fragmentary description of the interlayer, and particularly of its H-bonding network. Notably, a possible H-bond between the two central water molecules would preclude a P-1 symmetry at the local level, a point considered in more detail in this study.

Studies of OCP *via* solid-state NMR (ssNMR)[6,13,15,16] have offered more insight into its structure. Most importantly for the present work, a ^{1}H and ^{31}P high resolution NMR investigation by Davies *et al.*,[15] published in 2012, led to a revised structure of OCP, based on a combination of experimental assignments and first-principles calculations. This investigation sought to find a single structure that would simultaneously reduce the calculated strain on the structure through DFT relaxation, and could closely match the observed ^{31}P NMR parameters of OCP. Nonetheless, the authors had to deal with several issues: not only was the synthesised OCP contaminated with HAp, but experimental ^{31}P chemical shifts were also found to be dependent on temperature (varying by ~0.5 ppm over 100 K), suggesting possible mobility within the structure. Additionally, the ambiguous symmetry of previous studies remained, with the proposed structure having an assigned symmetry of $P1$, but with nearly identical atomic arrangements on either side of the cell. It was stated in the manuscript: "It is worth noting that the optimised structure is approximately consistent with P-1 symmetry (the maximum deviation from symmetry was determined by DFT to be 2.684×10^{-5} Å); however, given the slight inconsistencies between the atomic positions and the symmetry operations of P-1, it is taken to be a $P1$ system."[15] The choice of starting from a P-1 structure may have been made because the calculated ^{31}P NMR parameters on an asymmetric $P1$ cell showed strong splittings of the peaks, which is not consistent with ambient temperature ^{31}P experimental data. Nevertheless, the proposed structure was a compromise between a Rietveld-refined structure,[12] featuring unrealistic bond angles and lengths, and the more realistic simulated interatomic distances and angles given by DFT relaxation. It also enabled a fairly close match to experimental ^{31}P chemical shifts, although with a much larger error than that found for some related calcium phosphates ($CaH_2PO_4 \cdot H_2O$, $CaHPO_4 \cdot 2H_2O$).[17] It therefore proved that an NMR crystallographic study was valuable when studying the structure of OCP, including for the assignment of the structure's phosphorus sites. The study did not, however, solve the issues of symmetry, nor explain the changes in chemical shifts with temperature. The recent advances in isotopic labelling, NMR instrumentation (low-temperature magic angle spinning (MAS) probes and high-field NMR spectrometers), and computational modelling, now allow us to further push the scope of NMR crystallographic studies of OCP.

The current study aims at expanding our understanding of the hydrated interlayer space of OCP and its potential mobility, using a combination of variable-temperature NMR spectroscopy (including at temperatures as low as 100 K), and molecular dynamics (MD) simulations. First, two improved protocols for the reproducible synthesis of high-purity OCP are described, both at gram-scale and in scaled-down quantities, for the purpose of isotopic enrichment. Notably, we propose an economical synthesis of [17]O and [43]Ca enriched samples. These samples are then analysed by multinuclear ssNMR at ambient and low temperature, demonstrating the existence of a significant change in the NMR signature. The origin of these changes is investigated with the help of computational modelling (MD simulations). Lastly, a new description for the structure of OCP is proposed, taking into account the presence of molecular motions in the cell, and assignment of some of the resonances recorded in the different NMR spectra obtained throughout the study. Remaining difficulties related to the OCP structure are also discussed.

Experimental section

Materials and methods

Reagents

The following reagents were used as received: phosphorus pentoxide (P_2O_5, Sigma-Aldrich, ≥ 99 %), orthophosphoric acid (H_3PO_4, Honeywell, 85 % w/w in water), and non-labelled calcite ($CaCO_3$, Acros Organics, ≥ 99%).

[17]O-labelled water was purchased from Eurisotop, with a ~90% enrichment level. [43]Ca-enriched $CaCO_3$ was purchased from Cortecnet, with a ~60% enrichment level.

Gram-scale synthesis of octacalcium phosphate (OCP)

Octacalcium phosphate was synthesised in water by adapting previously published protocols.[16] Because OCP is a reaction intermediate in the transformation of dicalcium phosphate dihydrate (DCPD, $CaHPO_4 \cdot 2H_2O$) into HAp, a precise control over the reaction kinetics is required to obtain a pure product. Since the $CaCO_3$ precursor's solubility is linked to the concentration of CO_2 in the reaction medium, the following improvements were made: (i) suppressing the accumulation of CO_2 gas in the reaction medium by using a flow of argon and (ii) avoiding the accumulation of DCPD on the walls of the reaction medium (where it can remain unreacted). As such, the following protocol was employed for the gram-scale synthesis of unenriched OCP.

A 100 mL solution of H_3PO_4 (0.100 mol.L^{-1}, 10 mmol, 1 eq) was heated to 60°C in a 250 mL round-bottom flask under argon. $CaCO_3$ (1.38 g, 13.87 mmol, 1.37 eq) was then gradually added over 5 minutes. A dense white precipitate appeared rapidly after the addition of $CaCO_3$. The reaction medium was stirred for 6 hours at 900 rpm, during which a flocculent white solid gradually filled the volume of the reaction medium. The solid was then filtered over a Büchner funnel and washed three times with 10 mL of water, yielding a large mass (≈ 12 g) of white paste. The paste was dried at 50°C overnight (under air), leading to the loss of a significant mass of water (≈ 10.5 g). The synthesis yielded 1.55 g (1.74 mmol, 96% yield) of a fluffy white powder, which was identified as OCP via IR spectroscopy, pXRD, and ^{31}P ssNMR. The powder was stored at −20°C until further analysis.

Low-scale synthesis of [43]Ca-enriched OCP

A scaled-down protocol was developed for enriching OCP in either calcium-43 or oxygen-17. Given the high price and low availability of the enriched precursors, it was essential to reduce the synthesis scale while ensuring an optimal synthetic yield. To minimise losses in isotopically labelled product, all synthetic steps (precipitation, separation, washing and drying) were carried out in a single 50 mL round-bottom polypropylene centrifuge tube, as detailed below.

A 5 mL solution of H_3PO_4 (0.100 mol.L^{-1}, 0.508 mmol, 1 eq) in ultrapure H_2O was added to the tube, heated to 60°C in an oil bath, and stirred with a PTFE crosshead stirring bar up to 800 rpm. A mixture of [43]Ca-enriched Ca*CO_3 and non-enriched $CaCO_3$ powders (~ 71 mg total mass, 0.70 mmol, 1.37 eq) was rapidly added to the reaction medium, causing the immediate formation of a dense white precipitate. The tube was sealed with a septum and placed under an Argon atmosphere, by inserting two 0.80 mm diameter needles into the rubber septum (one for Ar inlet, the other for Ar outlet). The reaction medium was then stirred at 60°C for 6 hours, during which it was sonicated four times (at t+ 0:30, 1:00, 1:30 and 2:30), to homogenise the reaction medium and favour the release of "trapped"

CO$_2$ bubbles. At the end of the reaction, the reaction medium was completely filled by a white, watery paste. After cooling back to room temperature, the solid was then separated from the reaction medium *via* centrifugation at 20k rpm for 10 minutes, then washed twice using 5 mL of ultrapure H$_2$O. The residual powder was dried inside the centrifuge tube overnight at 50°C (under air). This reaction was run twice, once using an average ^{43}Ca-enrichment level of 5% for the starting CaCO$_3$, and the other of 15%. After drying, 80.9 mg and 78.4 mg of enriched OCP were isolated, which corresponds to synthetic yields of ca. 95% and 94%, respectively. The ^{43}Ca-enriched products were stored at −20°C. The estimated cost for the ^{43}Ca-labeling synthesis is ca. 900€ (for a 15% labelled sample, using ≈15 mg of enriched Ca*CO$_3$ precursor). As shown below, high quality 1D ^{43}Ca MAS NMR spectra were collected in just an hour.

Low-scale synthesis of ^{17}O-enriched OCP (with enrichment on the PO and POH groups)

OCP was enriched in oxygen-17 by synthesising a labelled H$_3$PO*$_4$ precursor and using it in the previously described protocol. 175.7 mg of labelled H$_3$PO*$_4$, was subsequently diluted in 1 mL H$_2$O to yield a concentrated orthophosphoric acid solution. 345 µL of this solution were then further diluted to yield an aqueous solution of H$_3$PO$_4$ (5 mL, 100 mM, 0.51 mmol, 1 eq), which was in turn used as a precursor for the synthesis of the oxygen-17 enriched OCP, by adding unlabelled CaCO$_3$ (67.6 mg, 0.68 mmol, 1.37 eq.), and then following the protocol described above for ^{43}Ca labelling. This produced 71.6 mg of labelled sample, with an 86% yield. The powder was stored at -20°C until further analysis. The enrichment of OCP in ^{17}O and ^{43}Ca was successful for both isotopes on the first attempt, and provided a relatively inexpensive way to observe these rare nuclei with much reduced experimental times. The estimated cost of the labelled precursor for the ^{17}O synthesis is ca. 65€. As shown below, high quality 1D ^{17}O MAS NMR spectra were collected for each nucleus in just an hour.

Infrared spectroscopy (IR)

IR analyses were performed on a Perkin-Elmer Spectrum 2 FT-IR instrument. The ATR mode was used for measurements ranging from 400 to 4000 cm^{-1}.

Powder X-ray diffraction (pXRD)

Room temperature pXRD analyses were performed on an X'Pert MPD diffractometer using CuK$_{\alpha 1}$ radiation (λ = 1.5406 Å), with the operating voltage and current maintained at 40 kV and 25 mA, respectively. X-ray diffractograms were recorded in Bragg-Brentano reflexion mode, in the 2θ range from 3° to 60°, and a step size of 0.017°.

Variable-temperature pXRD analyses were performed on a similarly configured X'Pert MPD diffractometer equipped with a cryogenic chamber and a kapton window. The temperature was first gradually lowered from ambient down to 100 K, then gradually increased back to ambient temperature, with steps of 20 K, and 45 minutes acquisitions. The temperature is given with a ± 5°C error.

SEM (Scanning Electron Microscopy), EDXS (Energy Dispersive X-ray Spectroscopy), and TEM (Transmission Electron Microscopy).

SEM and EXDS analyses were carried out on a Zeiss Evo HD15 scanning electron microscope equipped with an Oxford Instruments X-MaxN SDD 50 mm^2 EDXS detector. Before the SEM analyses, samples were deposited on a double-sided conducting carbon tape.

TEM images were recorded at 100 kV on a JEOL 1400 Flash instrument. Samples for TEM were prepared by depositing a suspension of the OCP particles (dispersed in 1:1 EtOH/H_2O by volume) onto carbon-supported copper grids and left to dry overnight at air, prior to analyses.

Solid-state NMR (ssNMR)

¹H solid-state NMR

A high resolution, high field, ^1H MAS NMR spectrum was acquired on the 35.2 T series connected hybrid (SCH) magnet at the National High Magnetic Field Laboratory (NHMFL, Maglab),[18] using a Bruker Avance NEO NMR spectrometer operating at a ^1H Larmor frequency of 1500.10 MHz, and a 1.3 mm narrow-bore NHMFL probe spinning at 50 kHz. The temperature was regulated to 0°C (temperature of the refrigerating unit). The spectrum was acquired using a Hahn-Echo sequence, with 90 and 180° pulse of 5 and 10 μs, respectively, separated by an echo delay of 1 rotor period (20 μs). A total of 8 scans were recorded with a recycle delay of 5 s.

Low and ambient temperature ^1H NMR experiments were performed at the CRMN Lyon on an 18.8 T Avance NEO spectrometer operating at a ^1H frequency of 799.66 MHz, equipped with a low-temperature 1.3 mm probe, achieving spinning rates of 40 kHz at ca. 100 K (temperature of the refrigerating unit). The room-temperature ^1H spectrum was acquired using a Hahn-echo sequence, with 90 and 180° pulse of 3.7 and 7.4 μs, separated by an echo delay of 1 rotor period. A total of 32 scans were acquired, using a recycle delay of 8 s (which corresponds to full relaxation at room temperature). The low-temperature (100 K) ^1H spectrum was acquired using a DEPTH background-suppression scheme, using 90° and 180° pulses of 2.25 and 4.5 μs, respectively.[19] A total of 16 scans were acquired with a recycle delay of 16 s (which does not correspond to full relaxation at 100 K, but the overall lineshape did not show significant difference between 16 and 64 s of recycle delay). ^1H chemical shifts were referenced to the OH group of crystalline HAp at 0.0 ppm relative to adamantane (at 1.8 ppm).

³¹P solid-state NMR

^{31}P MAS NMR experiments were performed at "close to ambient" temperature (temperature of the refrigerating unit set to 0°C), at 14.1 T on a Varian VNMRS spectrometer operating at ^1H and ^{31}P Larmor frequencies of 599.82 MHz and 243.12 MHz respectively, using a 1.6 mm HXY probe. The rotor spinning speed was set at 20 kHz. The Bloch decay, quantitative ^{31}P NMR spectrum was acquired with a recycle delay of 750 s over four scans, with a 100 kHz SPINAL-64 ^1H decoupling.

^1H – ^{31}P cross-polarisation (CP) experiments in DNP conditions were performed at cryogenic temperatures (down to 100 K), using an Avance III NMR spectrometer (9.4 T) operating at ^1H and ^{31}P Larmor frequencies of 400.00 and 161.92 MHz respectively equipped with a 263 GHz gyrotron for microwave irradiation, and a low-temperature 3.2 mm probe in double resonance (HX) configuration. Radio frequency (rf) field strengths were set to 71.4 kHz in the case of ^{31}P and 100 kHz on the ^1H channel. A series of ^1H-^{31}P CPMAS spectra at various temperatures were acquired without the presence of microwaves, with a CP contact time of 2 ms, a recycle delay of 5 s, and 8-16 scans per experiment at a MAS rate of 10 kHz, and using SPINAL-64 ^1H decoupling[20] during acquisition, with a ^1H decoupling power of 130 kHz. For DNP-enhanced NMR experiments, the sample was impregnated with a DNP matrix containing 10 mM of AsymPol-POK radical[21] in a 60/30/10 volume ratio of a d_8-glycerol/D_2O/H_2O mixture. The ^1H polarisation was then transferred to the ^{31}P nuclei using a CP sequence with a contact time of 2 ms. The recycle delay was set to 2.3 s according to the optimal ^1H-^{31}P polarization build-up time under microwave irradiation. DNP enhancements for all ^{31}P peaks

obtained in this configuration were of $\varepsilon_{on/off}$ = 29 (Fig. S1). Subsequently, a 2D ^{31}P-^{31}P Double Quantum/Single Quantum (DQ/SQ) spectrum was acquired, with double-quantum excitation and reconversion of the ^{31}P spins being achieved with the dipolar recoupling sequence S3.[22–24] The experimental temperature under microwave irradiation was approximately 100 K and the spinning speed was set to 13 kHz. A 100 kHz rf field strength ^1H decoupling was used during direct detection period utilising the SW_f – TPPM decoupling scheme,[25] whereas a 100 kHz rf SPINAL-64 scheme and continuous wave irradiation was used for the indirect detection period and the S_3 recoupling block, respectively. 256 points containing 16 transients each were acquired, corresponding to a total experimental time of approx. 2.5 h, with a mixing time of 7.4 ms. A ^1H – ^{31}P CP-HETCOR correlation spectrum was also recorded under identical DNP conditions. Enhancement was achieved by transferring magnetisation from the hyperpolarised proton with a CP contact time of 0.2 ms. The indirect acquisition was obtained with 196 slices with 8 scans each, with a 2.34 s recovery delay between each transient, for a total experimental time of 1 h. An FSLG decoupling scheme was applied during the evolution time (100 kHz rf field), while a SW_f – TPPM ^1H decoupling scheme was applied during the acquisition (100 kHz rf field).

High-field ^{31}P MAS NMR experiments were recorded at low temperature (ca. 100 K – temperature of the refrigerating unit) using the 18.8 T Avance NEO spectrometer at ENS Paris, operating at ^1H and ^{31}P Larmor frequencies of 800.23 and 323.94 MHz respectively, and equipped with a low-temperature 3.2 mm probe, spinning at 8 kHz. A direct-excitation ^{31}P NMR spectrum was recorded with a 30° pulse (1.6 µs, 52 kHz rf), and SPINAL-64 ^1H decoupling during acquisition (ca. 70 kHz rf field strength). The recycle delay was set to 200 s, and 24 scans were acquired (T_1 was not measured precisely, but no change in relative intensities of the different OCP ^{31}P signals was observed when using recycle delays of 60 s or 400 s). ^{31}P CPMAS NMR spectra were recorded using a 90° (4.8 µs, 52 kHz rf) excitation pulse on the ^1H, an array of contact times from 0.15 to 5.45 ms with 0.10 ms increments, and applying SPINAL-64 ^1H decoupling during acquisition (52 kHz rf); the recycle delay was set to 60 s, and 16 scans were acquired at each contact time. ^{31}P chemical shifts were referenced to the phosphate peak of crystalline HAp at 2.8 ppm or to an 85% H_3PO_4 solution at 0.0 ppm.

^{17}O high-field solid-state NMR
An ultra-high field ^{17}O MAS NMR spectrum was recorded at the NHMFL in Tallahassee on the SCH magnet at 35.2 T, using a Bruker Avance NEO NMR spectrometer operating at ^1H and ^{17}O Larmor frequencies of 1500.10 and 203.36 MHz respectively. A NHMFL 1.3 mm narrow-bore solid-state NMR probe was used, spinning to 25 kHz. The spinning speed was chosen to minimise the overlap of spinning sidebands with the sample signal. The sample temperature was regulated to 0°C (temperature of the refrigerating unit). The spectrum was acquired using a Hahn-echo sequence, with central-transition (CT)-selective pulses (8 µs excitation and 16 µs refocusing pulses; for a power of 3.125 W) and an echo delay of 1 rotor period. The recycle delay was set to 1 s and 4096 scans were recorded. No decoupling was applied during the acquisition.

A 2D ^1H – ^{17}O correlation experiment was also recorded at the NHMFL, on an 18.8 T Bruker spectrometer operating at ^1H and ^{17}O Larmor frequencies of 799.71 and 108.42 MHz respectively, equipped with a low-temperature 1.3 mm probe, spinning at 50 kHz under ambient conditions. A D-RINEPT-based magnetisation transfer[26] was used, with the $SR4_1^2$ based recoupling sequence.[27] On the ^{17}O channel, a WURST pulse was first applied (1 ms length, with a power of 8 W), followed by a 4 µs CT-selective pulse (corresponding to ca. 21 kHz rf field strength for the liquid). On the ^1H channel, the

total $SR4_1^2$ recoupling time was 480 µs. The recycle delay was set to 0.15 s. A total of 64 complex t_1 increments with 1792 transients were acquired. The total experimental time was ca. 10 h. No decoupling was applied during the acquisition.

Low and ambient temperature ^{17}O NMR experiments were performed at the CRMN Lyon on an 18.8 T Avance NEO spectrometer operating at ^1H and ^{17}O Larmor frequencies of 799.66 and 108.42 MHz respectively, equipped with a low-temperature 1.3 mm probe, spinning at 25 kHz. ^{17}O NMR spectra were recorded with a double frequency sweep (DFS)[28] enhancement scheme. The DFS-sweep had a length of 400 µs, starting at a frequency offset of 200 kHz and ending at 70 kHz; the power of this pulse was 10 W at ambient temperature, and 5 W at 100 K. The DFS pulse was followed by an excitation pulse of 2.33 µs at ambient temperature (1.5 µs at 100 K). No decoupling was applied on the ^1H channel (when applying ^1H decoupling at 100K, the PO region remains essentially unchanged, while the relative intensity of the POH region only increases by less than 15%). At both temperatures, the recycle delay was set to 1 s, and 24000 scans were acquired. A 2D $^1H – ^{17}O$ correlation experiment was also recorded at 100 K (temperature of the refrigerating unit), spinning at 30 kHz, and using a D-HMQC (dipolar-heteronuclear multiple-quantum coherence) sequence with the $SR4_1^2$ recoupling scheme.[27] The 90° pulses applied on the ^{17}O and ^1H were of 2.33 and 2.5 µs duration, respectively. The total $SR4_1^2$ recoupling time was 276 µs. The recycle delay was set to 0.8 s. A total of 62 slices with 3528 scans each were acquired, for an experimental time of ca 50 h. ^{17}O chemical shifts were referenced to water (H_2O) at 0.0 ppm.

^{43}Ca high-field solid-state NMR

^{43}Ca MAS NMR experiments at ambient temperature were performed at multiple magnetic fields (18.8, 23.4 and 35.2 T) at different NMR facilities (ENS in Paris, UK NMR facility in Warwick, and NHMFL in Tallahassee). All were direct ^{43}Ca acquisitions on an enriched compound. The 35.2 T acquisition was recorded using a 5% enriched sample, whereas the others were recorded on a 15% enriched sample.

The 35.2 T spectrum was recorded on the NHMFL SCH magnet, using a Bruker Avance NEO NMR spectrometer operating at the ^{43}Ca Larmor frequency of 100.96 MHz, using a NHMFL 3.2 mm probe spinning at 10 kHz, and setting the refrigerating unit to 10 °C. A total of 24634 scans were acquired with a recycle delay of 0.5 s, for an acquisition time of ca. 3h30. A DFS enhancement scheme was used, with a starting offset of 400 kHz, sweeping down to 50 kHz over 5 ms with a set power of 5 W. The DFS was followed by an 8 µs excitation pulse (31 kHz, solid 90°). A multi-DFS enhancement scheme[29] was applied, with four acquisitions per recycle delay. No decoupling was used during the acquisition.

The 23.4 T spectrum was recorded using an Avance NEO 1000 spectrometer, operating at the ^{43}Ca Larmor frequency of 67.66 MHz, and equipped with a 1.9 mm probe spinning at 40 kHz, while setting the temperature of the refrigerating unit to 0°C. The DFS swept from an offset of 400 kHz to 50 kHz and had a duration of 2 ms and a set power of 10 W. The DFS was followed by a 1.8 µs excitation pulse (corresponding to a 22.5° tilt angle on a liquid). A total of 17848 scans were acquired with a recycle delay of 1 s, for an acquisition time of 5 h. No decoupling was used during the acquisition.

At 18.8 T, a low-temperature 3.2 mm probe was used, allowing for acquisitions both at room temperature and at 100 K using similar experimental parameters. The spectra were recorded with an Avance NEO spectrometer operating at a ^{43}Ca Larmor Frequency of 53.86 MHz, using a low-temperature MAS probe spinning at 8 kHz. At both temperatures, a DFS enhancement scheme was used, with a 2 ms sweep duration (20 W power), starting with an offset of 400 kHz down to 50 kHz. This pulse was followed by a 3.75 µs excitation pulse (150 W power, corresponding to ca. 16 kHz rf on the liquid). No decoupling was used during the acquisition. Acquisitions at both temperatures were

performed with a recycle delay of 0.8 s. A total of 55068 scans were acquired at ambient temperature, and 34088 scans at 100 K. ^{43}Ca chemical shifts were referenced to a 1M $CaCl_2$ solution at 0.0 ppm.

Processing and fitting of the ^{31}P CPMAS build-up curves

The series of 54 ^{31}P CPMAS NMR spectra with varying contact times which had been recorded at 100 K were fitted sequentially using a sum of Pseudo-Voigt peaks. This was done using a homemade Python script, with the nmrglue[30] and scipy[31] modules for data reading and fitting respectively. The fit was optimised using the Levenberg-Marquardt method from the "curve_fit" function of the scipy module. The amplitudes of all component peaks were set as variables, and all other parameters (peak width, g/l ratio and position) were fixed. The value of the amplitude of each peak was estimated for each spectrum of the series, and the error calculated from the square root of the diagonalised covariance matrix. The values of the peak amplitudes over the contact time (t_{cp}) were then fitted with the simplified expression:[32]

$$I(t_{cp}) = \frac{I_0}{1 - T_{cp}/T_{1\rho}}(e^{\frac{-t_{cp}}{T_{1\rho}}} - e^{\frac{-t_{cp}}{T_{cp}}})$$

with I_0 the absolute amplitude of the resonance, T_{cp} the time constant of the magnetisation transfer and $T_{1\rho}$ the simplified time constant of the spin-lattice relaxation. In cases where $T_{1\rho}$ was large (> 50 ms) in comparison to the longest contact time recorded (5.55 ms), it was considered infinite and the terms scaling with a factor of $T_{1\rho}^{-1}$ were nullified. The optimised values and errors for I_0, T_{cp} and $T_{1\rho}$ were likewise obtained using a Levenberg-Marquardt minimisation algorithm.

DFT calculations

Molecular dynamics simulations and averaging

Two molecular dynamics simulations were performed starting from the DFT-relaxed structure obtained in the previously published NMR-crystallography study of OCP by Davies *et al.*[15] The calculations were done using the CP2K package,[33] consisting in Born–Oppenheimer MD (BOMD) with PBE electronic representation, including the Grimme (D3) correction for dispersion,[34] GTH pseudopotentials,[35] combined plane-wave, and TZVP basis sets.[36] The simulation was carried out over 30000 steps, with a step time of 0.5 fs in an NVT canonical ensemble, periodic boundary conditions, fixed cell parameters and unconstrained atomic positions. For the calculation of the forces, we used a QUICKSTEP method with an analytical stress tensor and an energy cut-off of 400 Ry. The temperature of the ensemble was set using a Nosé-Hoover-chain thermostat[37] composed of three elements, with a set temperature of 100 K in the first MD simulation, and 300 K in the second. Although the initial structure exhibits a *P*-1 symmetry, no symmetry constraints were imposed during the simulation. Averaged structures of OCP over the 100 K and 300 K MD simulations were obtained by averaging the atomic positions of a given atom at each step of the MD (from step 1000 to 30000). Recordings of the 10000 first steps of both MD simulations are available as supplementary files.

NMR computations

GIPAW calculations were performed with the QUANTUM-ESPRESSO[38] software, using a DFT formalism with a PBE gradient approximation.[39] The valence electrons were approximated using a norm-conserving pseudopotential. The wave functions are expanded on a plane wave basis set with a kinetic energy cut-off of 80 Ry with a Monkhorst-Pack grid of 1 × 2 × 3. For this study, the numbering

of the sites is made consistent with a previously published structure.[15] Calculated NMR parameters over the duration of the MD simulations were determined by averaging the predicted shielding and electric field gradient tensors over a set number of evenly spaced structures. For this purpose, a GIPAW calculation was performed every 100 steps for the duration of the molecular dynamics simulation, starting from step 1100, for 290 GIPAW calculations per simulation. Time-averaged δ_{iso} values, calculated for each step, are the mean average of all δ_{iso} up to the specific time step. The principal components of the EFG tensor for a given site were then obtained by first averaging each individual components of the EFG tensor over the length of the simulation, and then diagonalising the averaged EFG tensor following the convention $|V_{zz}| \geq |V_{xx}| \geq |V_{yy}|$. The quadrupolar interaction is given with the values $C_Q = eQV_{zz}/h$ and $\eta_Q = (V_{yy} - V_{xx})/V_{zz}$, with the quadrupole moments Q taken from recent experimental measurements ($Q_{17O} = -25.58$ mb, $Q_{43Ca} = -44.4$ mb).[40,41,42] Based on C_Q and n_Q, the P_Q parameter which is also used in this contribution is defined by $P_Q = C_Q \left(1 + \frac{\eta_Q^2}{3}\right)^{1/2}$. All of the data treatment was facilitated using homemade Python scripts, using the Numpy[43] module for all numerical applications.

The isotropic chemical shift δ_{iso} is defined as $\delta_{iso} \approx -(\sigma_{iso} - \sigma_{ref})$, where σ_{iso} is the isotropic shielding and σ_{ref} is the isotropic shielding for the same nucleus in a reference system. σ_{ref} was referenced internally as the difference between the average calculated σ_{iso} and chemical shift values of the best resolved 300 K experimental spectra. Here, $\sigma_{ref}(^1H) = 29.9$ ppm; $\sigma_{ref}(^{31}P) = 288.3$ ppm; $\sigma_{ref}(^{17}O) = 230$ ppm; $\sigma_{ref}(^{43}Ca) = 1110$ ppm. Note that the reference value for oxygen-17 is close to the one recently used for calcium oxalates[44] and characteristic of the presence of Ca-O bonds leading to a partial Ca-3d O-2p hybridisation.[45]

Results

Syntheses and characterisations at ambient temperature

All syntheses (both gram-scale and low-scale) were tested for reproducibility and led to a crystalline OCP phase as confirmed by pXRD analysis (Fig. S2). The main obstacles to a successful synthesis are the incomplete or excessive transformation of the DCPD precursor, leading to DCPD or HAp impurities, respectively. Whereas DCPD can easily be distinguished from OCP from its XRD powder pattern, HAp has similar diffraction peaks (in the intermediate angular range) and is more easily differentiated in ^{1}H ssNMR spectra, where its OH resonance is found at 0.0 ppm (on a ^{31}P spectrum, the HAp resonance is broad and centered at ca. 2.8 ppm). The Ca/P ratio of the compound synthesised via the scaled-up synthesis was estimated to be 1.41 ± 0.06 via EDXS microanalysis (Table S1), which is slighty above the theoretical value of 1.33, and to the ratio of the precursors during the synthesis (1.37). The Ca/P ratio of stoichiometric HAp is 1.67, and that of DCPD is 1.00. These observations lead us to believe that the OCP synthesised through these methods is of relatively good purity, with a possible presence of small amounts of HAp and/or $CaCO_3$ impurities. The samples were also analysed by SEM and TEM (Fig. S3), showing platelets characteristic of OCP. These are polydisperse, with particle lengths ranging from hundreds of nanometers to several micrometers. We note the extremely variable size and shape of the platelets, which may explain the variable relative intensities of different diffraction peaks obtained in XRD analysis for the different samples (Fig. S2a). In the case of the ^{17}O-enriched sample, the success of the enrichment could be confirmed *via (i)* ATR-IR spectroscopy, where the increased atomic weight

of the oxygen isotopes leads to lower frequency resonances for P-O vibration modes (e.g. bands at 1020 and 560 cm^{-1}) (Fig. S2b), *(ii)* ^{31}P CPMAS NMR, where the additional ^{17}O-^{31}P couplings lead to changes and broadenings of the ^{31}P resonances, in comparison to the non-labelled compounds (Fig. S3c), and *(iii)* ^{17}O MAS NMR, as discussed later in this article.
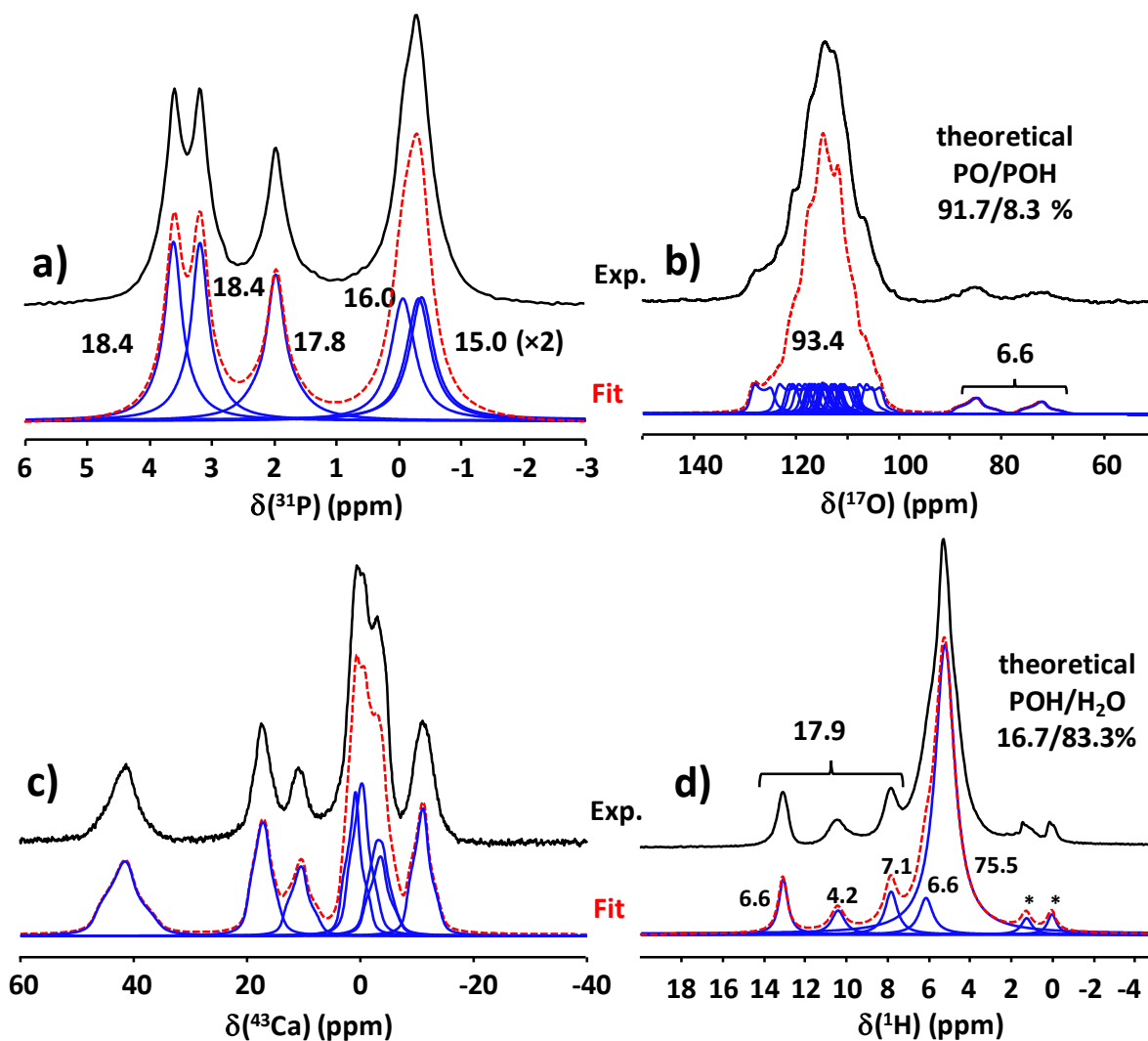
Figure 2: Experimental (black) and fitted (red dashed) MAS NMR spectra of OCP : a) ^{31}P single pulse spectrum recorded on the unenriched sample at B_0 = 14.1 T, v_r = 20 kHz (refrigerating unit set to 0°C) ; b) ^{17}O Hahn-Echo spectrum, refocused over one rotor period, recorded on the ^{17}O enriched sample, B_0 = 35.2 T, v_r = 25 kHz (refrigerating unit set to 0°C) ; c) ^{43}Ca direct-excitation spectrum, recorded on the ^{43}Ca enriched sample, B_0 = 35.2 T, v_r = 10 kHz (refrigerating unit set to 10°C) ; d) ^{1}H Hahn-Echo spectrum, refocused over one rotor period, and recorded on the ^{17}O enriched sample, B_0 = 35.2 T, v_r = 50 kHz (refrigerating unit set to 0°C). Relative proportions of signals (in %) are indicated in black. All NMR parameters used for fitting are summarised in Tables S2 to S4. (Two small ^{1}H resonances, indicated by the "*" symbol are visible at ~ 0 and 1 ppm, which a priori do not belong to OCP; the former one is tentatively assigned to HAp).

The ^{31}P MAS NMR spectrum of (non-labelled) OCP was recorded by direct excitation using a long recycle delay to enable relaxation of the different ^{31}P sites (Fig. 2a). It could be decomposed into six resonances (as expected from the reported crystal structure), with integrated areas proportional to

the amount of underlying sites, and considering three of the resonances almost superimposed, as already reported in previous NMR studies.[15]

The ^{17}O MAS NMR spectrum was recorded at 35.2 T (Fig. 2b). It clearly shows a main component ranging from 105 to 130 ppm (corresponding to PO sites), and two very distinct signals with δ_{iso} around 75 and 90 ppm respectively, accounting for about 6.6 % of the total signal. These can be safely assigned to the two POH environments expected in OCP. The P-OH/PO ratio is slightly lower than the expected value, possibly due to differences in T2 relaxation and/or in nutation rates of both types of sites during the spin-echo. The H_2O molecules of the interlayer were not enriched, and therefore are not visible in ^{17}O NMR under these conditions; their possible signature in ^{17}O NMR will thus not be discussed here. A tentative fit of the spectrum in the PO region could be proposed based on a two-field simulation (B_0 = 35.2 T and 18.8 T), with 22 components of similar intensities and using similar quadrupolar parameters for all sites (Fig. S4), i.e. with C_Q = 4.8 MHz and η_Q = 0.2 values, as suggested by later experiments (Fig. 9), and in reasonable agreement with previously reported values.[46–48]

At 35.2 T, the ^{43}Ca MAS NMR spectrum is still not fully resolved (Fig. 2c). Yet, it is consistent with the superposition of eight ^{43}Ca resonances, with some still slightly broadened by second-order quadrupolar effects. A tentative fit can be offered based on a multiple-field simulation with eight components (Fig. S5). It should be noted that this spectrum is close to the ^{43}Ca DOR (DOuble Rotation) NMR data previously reported in the literature.[16]

Finally, the ^1H MAS NMR spectrum (Fig. 2d) shows a main component centered about 4.5 ppm due to water molecules, and 3 minor signals around 13, 10 and 8 ppm consistent with POH sites involved in different H-bonds (presumably showing H---O distances ranging from 1.4 to 1.7 Å).[49] The presence of three signals compared to the two expected POH sites suggests a possible more complicated structure for OCP, as discussed below.

Temperature and dynamics effects

The ^{31}P CPMAS NMR spectra of OCP at low temperatures show a significant change compared to room temperature. Between 220 K and 100 K, the four main peaks observed at room temperature (corresponding to six inequivalent sites, consistent with a *P*-1 cell symmetry) gradually split into a larger number of resonances, with at least ten individually resolved sites (Fig. 3a). During subsequent observations, these temperature-dependent changes were found to be fully reversible and repeatable over multiple OCP samples, prepared using both gram-scale and low-scale synthesis protocols. Further studies included the observation of OCP at low and ambient temperature *via* ^1H (Fig. 3b), ^{17}O (Fig. 3c) and ^{43}Ca (Fig. 3d) NMR, using enriched samples. ^1H resonances are much broader at 100 K, suggesting a reduction of mobility of the different OH groups compared to ambient temperature. Although ^{17}O and ^{43}Ca NMR spectra also show an evolution of the signal between 100 K and close to ambient temperature, the most obvious changes were for the ^1H and ^{31}P NMR spectra.

To go one step further, a series of XRD powder patterns were recorded, ranging from 100 K to 280 K in steps of 20 K (Fig. S6). No evidence of a sudden change in OCP's complex pattern at any specific temperature was observed. Instead, a gradual shifting of the peaks occurred, consistent with a small change of the crystal cell parameters with temperature. This led us to hypothesise that the new signals observed in ^{31}P NMR were not the result of the appearance of a new phase or polymorph, but instead of a modification within the interlayer space caused by the change in temperature.
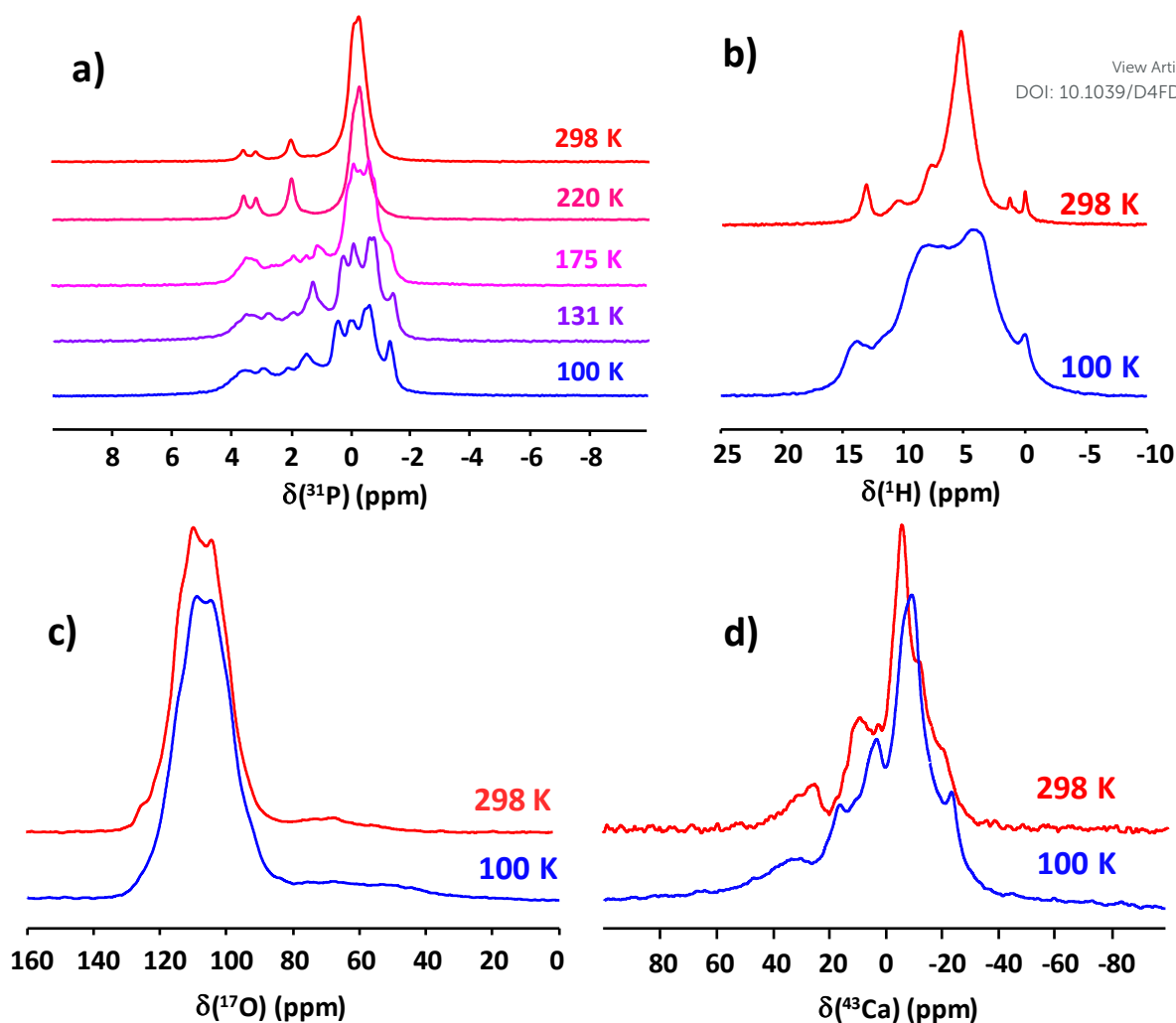
Figure 3: Evolution with temperature of a) ^{31}P CPMAS NMR spectra recorded on the unenriched OCP sample (B_0 = 9.4 T and v_r = 10 kHz, b) ^1H MAS NMR spectra recorded on the ^{17}O enriched OCP sample (B_0 = 18.8 T and v_r = 40 kHz), c) ^{17}O Hahn-Echo NMR spectra (refocused over one rotor period), recorded on the ^{17}O-enriched OCP sample (B_0 = 18.8 T and v_r = 25 kHz) and d) ^{43}Ca MAS NMR spectra recorded on the 15% ^{43}Ca-enriched OCP sample (B_0 = 18.8 T and v_r = 8 kHz). Indicated temperatures are those of the refrigerating units.

As mentioned in the introduction, previous studies[8,12] investigating the structure of OCP have had issues determining its symmetry group. With a high atom count, poor symmetry and a cluster of water molecules in the interlayer that are difficult to locate *via* X-ray diffraction, the presence of central symmetry in the cell remained a hypothesis. A high-resolution, room temperature observation of OCP *via* ^{31}P ssNMR seemingly confirms the *P*-1 symmetry group, as we only observe four distinct peaks, corresponding to the six equivalent positions of the lower symmetry (Fig. 2a). This is no longer true when observing OCP at temperatures below 175 K. Several mechanisms that may explain a symmetry break at low temperatures were considered in the literature: i) the asymmetric deprotonation of a water molecule to protonate a hydrogen phosphate (P6),[12] ii) the shifting of the position of a water molecule (whose oxygen atom is noted O19/O19', and has been shown to have high thermal parameters in previously reported XRD refinements),[12] or iii) the formation of an H-bond between the two central water molecules of O23 and O23' (Fig. 4).[12]

13
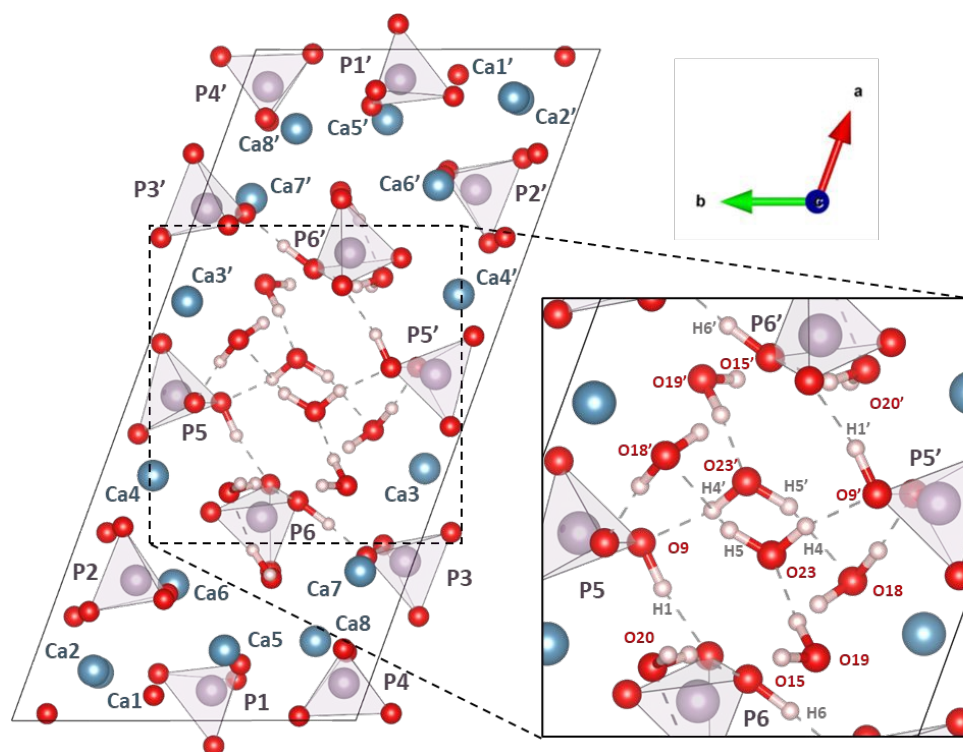
Figure 4: DFT relaxed OCP structure,[15] *with labels for calcium and phosphorus atoms (left) and relevant oxygen and hydrogen atoms of the interlayer (right). Each site is labelled with or without prime symbols, depending on its side relative to the cell's inversion centre.*

All these hypotheses are examined here, because they have been put forward in previous studies,[12,14] and are compatible with the observations by both XRD and NMR. As previous ssNMR analyses of OCP had shown the usefulness of *ab initio* calculations to help rationalise the experimental NMR spectra,[15,16] GIPAW calculations were also carried out as part of our work.

DFT relaxation and molecular dynamics simulations

A first series of numerical calculations were performed to investigate the possibility of explaining the symmetry break solely using "static" DFT relaxed-structures: GIPAW calculations of NMR parameters were performed on each model, and compared to the experimental data. A series of models were generated by selecting different relaxation parameters (relaxation of atomic positions only, or atomic positions and cell parameters). This did not result in a significant improvement of the calculated NMR parameters compared to the previously reported ones,[15] nor in any "spontaneous" loss of symmetry from an initial *P*-1 structure, once the symmetry constraints removed. Instead, we observed that a DFT relaxation starting from a *P*-1 structure but without symmetry constraints would systematically produce a *P*-1 symmetrical structure, as already reported.[15]

Because of the difficulties of investigating potential temperature effects using static models of OCP, two molecular dynamics simulations were run, at 100 K and 300 K (which are relevant temperatures based on our experimental ^{31}P NMR results). Starting from the same initial structure as for DFT relaxations (*P*-1 symmetry),[15] we simulated motions of all atoms in the structure, without any

symmetry constraints, nor any change to the cell parameters. The GIPAW NMR parameters were then calculated every 100 steps, and averaged over the whole simulation, as previously described.[50]

At 100 K, a significant symmetry break was observed within the first 1000 steps (0.5 ps): the two central water molecules nearest the symmetry center (O23, O23') break symmetry to form an H-bond from O23-H4 to O23' (Fig. 5). This H-bond has an average H···O length of 1.95 Å, and remains stable at least at the time scale of this simulation (15 ps) (See Fig 6a and 6b). Because it requires the rotation of the O23 water molecule, this also breaks the H-bond present in the XRD-refined structure[12] between H4 and the hydrogen phosphate oxygen O9' (Fig. 5). Hence, this motion breaks the *P*-1 symmetry of the initial structure and leads to a stable *P*1 symmetry over the length of the simulation.
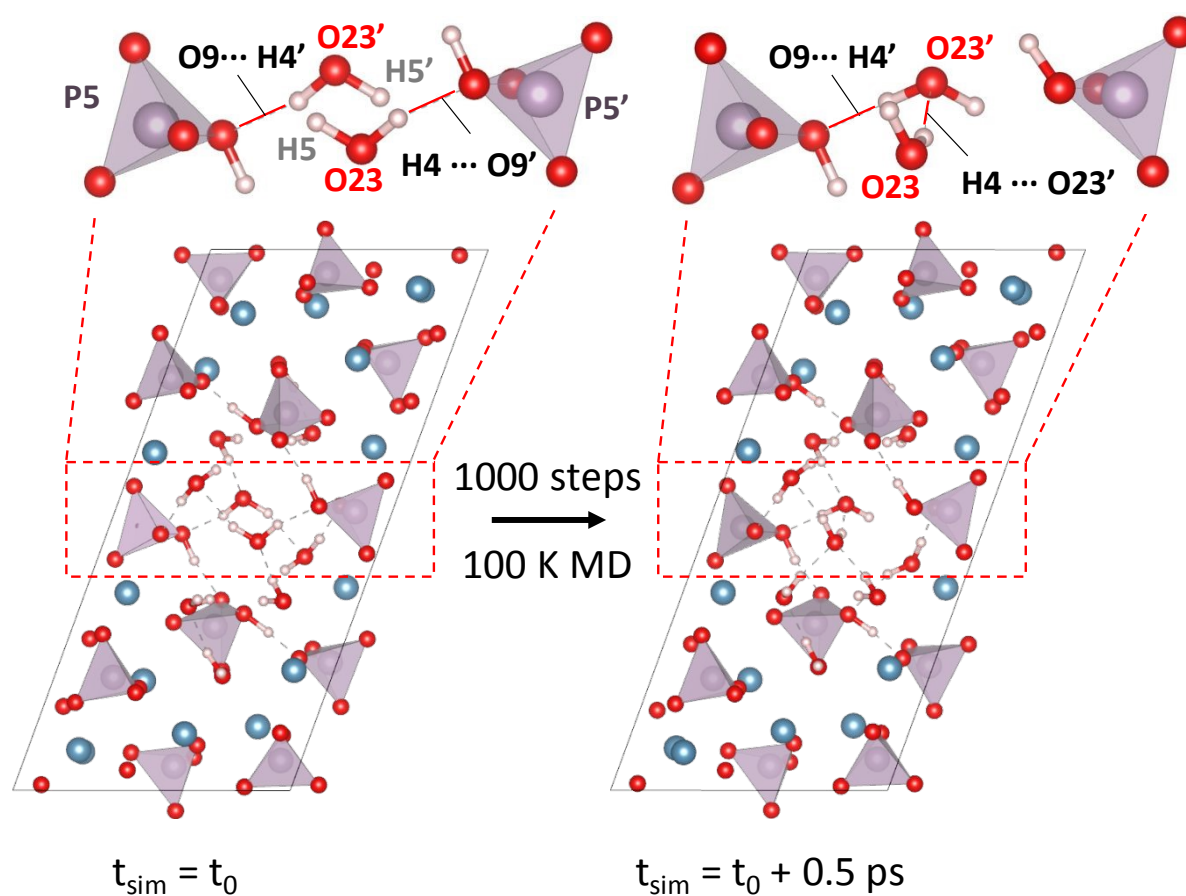

$t_{sim} = t_0$ $t_{sim} = t_0 + 0.5$ ps

Figure 5: Water molecule rotation inducing a symmetry break observed in the 1000 first steps of the 100 K molecular dynamics simulation.

At 300 K, the simulation starts similarly, with the formation of an H-bond between O23-H4 and O23'. However, at this temperature, the bond is not stable over time. Instead, it breaks and reforms asymmetrically multiple times throughout the simulation, as evidenced by the evolution of the bond lengths on opposite sides of the initial symmetry center (Fig. 6c and 6d).
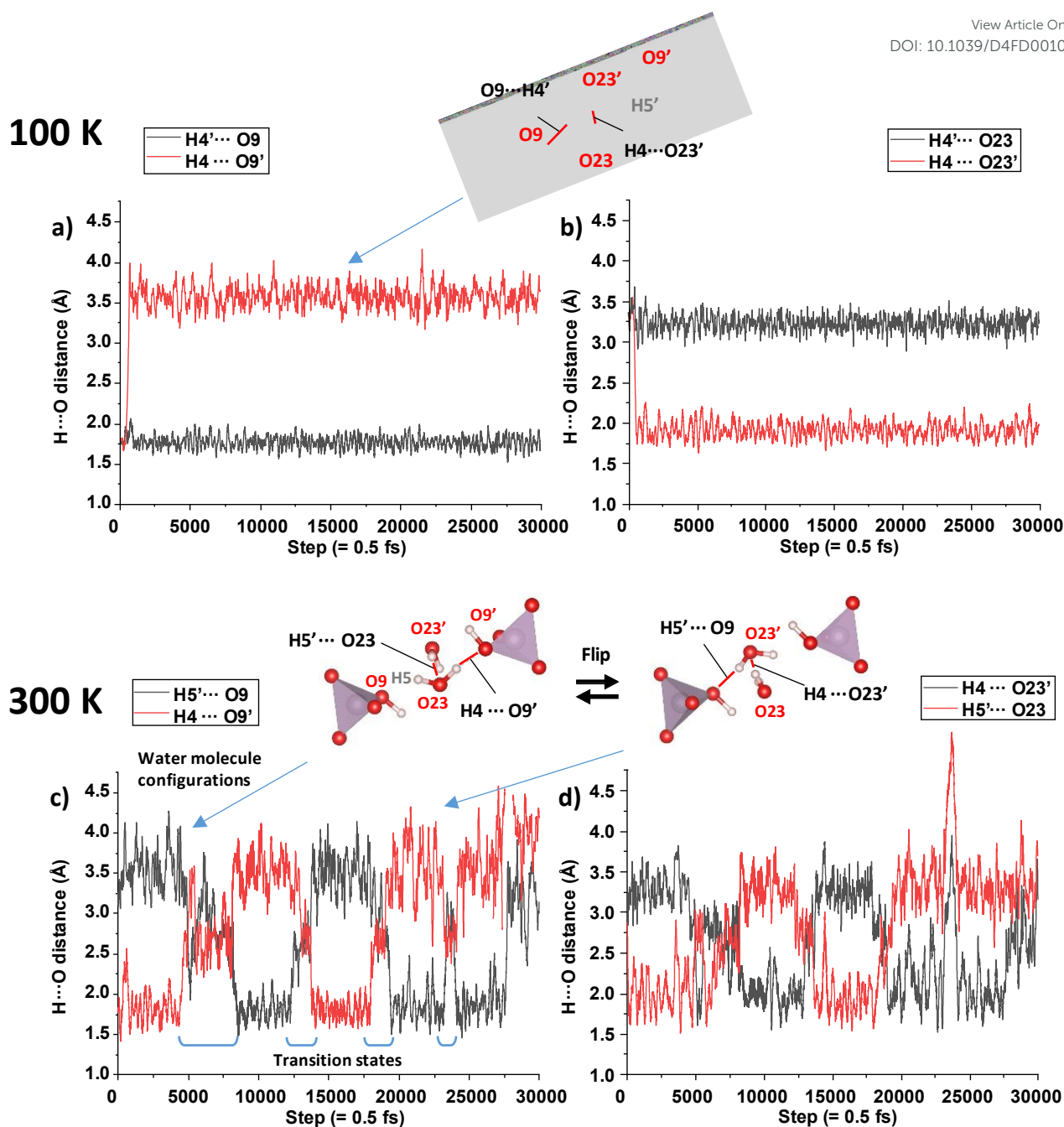
Figure 6: Evolution of H-bonds starting from the central water molecules (H4-O23-H5 and H4'-O23'-H5') over the molecular dynamics simulations. a) H-bond with the nearest HPO_4^{2-}, at 100 K. b) H-bond with the symmetrically opposed water molecule, at 100 K. c) and d) show the same H-bond types, but at 300 K. Representations of the different water molecule configurations observed in the simulations are shown above the graphs. Note that the H4'-O23'-H5' water molecule rotates in opposite directions at the beginning of the MD simulations we performed at 100 K and 300 K, thereby "inverting" the roles of H4' and H5'. The simultaneous increased distances of the H4···O23' and H5'···O9 bonds observed at the end of the MD at 300 K comes from 180° flips of the H4-O23-H5 water molecule. Recordings of the 10000 first steps of both MD simulations are available as supplementary files.

16

This "flipping" motion has little visible impact on the total energy of the system (Fig. S7). Given that we observe four flips over a 15 ps simulation, we can approximate a frequency of the order of ca. 10^{12} Hz at room temperature. We can also note the appearance of an intermediate structure during the symmetry transition that exhibits the *P*-1 symmetry which is not observed at 100 K. About 25% of the length of the simulation is spent in this transitional metastable *P*-1 symmetry. We can therefore describe this simulation as an alternation of symmetric and asymmetric structures (each lasting a few hundreds of fs) which averages out to a pseudo *P*-1 symmetry at 300 K. This is in contrast with the stable *P*1 structure observed at 100 K. The fact that the symmetry is related to water mobility, which is dependent on temperature, would explain why the temperature changes observed *via* ^{31}P NMR are gradual and fully reversible (and not visible in pXRD). Moreover, these simulations suggest that dynamics possibly affect NMR parameters of the phosphates in the hydrated interlayer (P3, P5 and P6) more strongly than those embedded further in the apatitic layers. This hypothesis will be used later in the manuscript when trying to assign the ^{31}P NMR spectra.

Averaged chemical shift calculations and effect of the water dynamics on NMR parameters

As shown in Figure 3, we were able to record ssNMR spectra for each isotope at both room- and low-temperature. We thus compared them with the calculated averaged NMR parameters from MD simulations. First, regarding ^{31}P NMR, the calculated isotropic chemical shifts of each ^{31}P site were found to progressively converge towards a given value during the length of the MD simulation (15 ps), as shown in Figure 7. Indeed, after 30000 steps, we observe that whereas the individual snapshots can still show variations of chemical shifts as high as 30 ppm (Fig. S8), the time-averaged values converge towards a much smaller range, varying by less than 0.5 ppm in the last 10000 steps, at both temperatures (Fig. 7a and 7b). Importantly, the 100 K MD simulation exhibits a major difference compared to the 300 K simulation. Indeed, as shown in Fig 7d, the average differences in the ^{31}P chemical shifts calculated at 100 K for P3/P3', P5/P5' and P6/P6' on both sides of the water interlayer are higher compared to those of the three other P sites (atoms labelled with or without a "prime" symbol on Fig. 4 are equivalent by *P*-1 symmetry). In contrast, in the simulation performed at 300 K (Fig. 7c), the average differences between Px and Px' chemical shifts converge towards zero for all sites, although slightly less completely for the P3 and P6 sites. Overall, these results are in line with both the splitting observed in ^{31}P low-temperature NMR spectra as well as the observed *P*-1 symmetry at ambient-temperature.
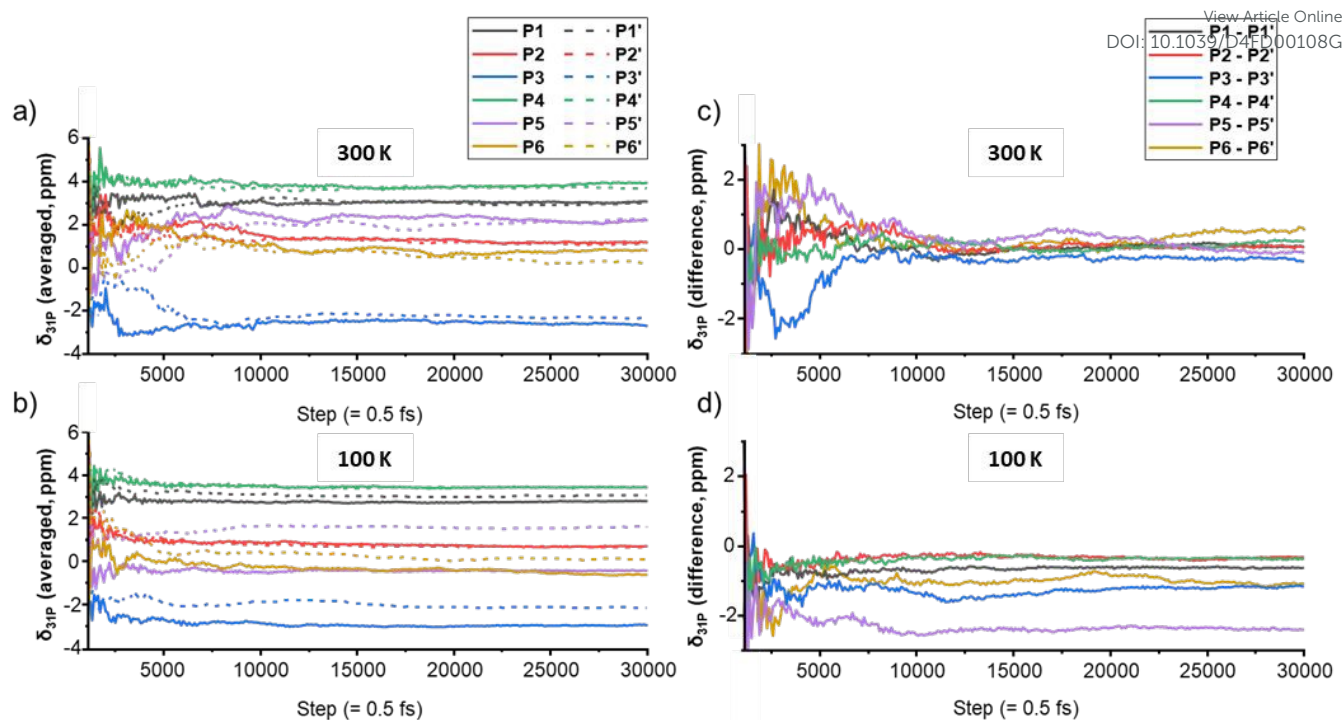
Figure 7: Evolution of the time-averaged GIPAW-calculated ^{31}P NMR isotropic chemical shifts a) at 300 K and b) at 100 K over the MD simulation. Difference in calculated ^{31}P chemical shifts for a given site on both sides of the interlayer (Px and Px') c) at 300 K and d) at 100 K. It can be noted that the difference between Px and Px' chemical shifts is negative for every site of the 100 K simulation. Explanation of the averaging mode is detailed in the experimental part.

 Yet, the MD-averaged ^{31}P NMR chemical shifts only partially agree with the experimental ^{31}P NMR data at 300 K (Fig. 8a vs c). At this stage, it should be recalled that a first assignment of the experimental ^{31}P MAS NMR spectrum of OCP had been proposed by Chan and co-workers in 2004,[13] based on the proximities established from ^{31}P-^{31}P DQ-SQ and ^{1}H-^{31}P CP-HETCOR experiments, but the proposed attribution (peaks at 3.7, 3.3, 2.0 and −0.2 ppm corresponding to P1, P2+P4, P3, P5+P6) did not match the experimental 1:1:1:3 intensity ratios observed in direct-excitation ^{31}P NMR spectra (Fig. 2a). A new attribution was later proposed by Davies *et al.* in 2012, based on DFT calculations and ^{31}P POST-C7 SQ−DQ correlation experiments with peaks at 3.6, 3.2, 2.0 and −0.3 ppm corresponding to P4, P1, P2, P3+P5+P6 (Fig. 8a),[15] which was consistent with the quantitative ^{31}P NMR data. Nonetheless, even if a satisfactory agreement was globally observed between experimental and calculated ^{31}P values with this new assignment,[15] the P3 position was still calculated at −1.9 ppm (Fig. 8b) which is still far from the expected −0.3 ppm. Note that as previously mentioned, Davies *et al.* had observed experimental ^{31}P chemical shifts to be dependent on temperature (increasing by ∼0.5 ppm over 100 K) and ^{31}P reported calculated values (Fig. 8b) were extrapolated at 298 K from the 0 K raw data. Here, averaging ^{31}P isotropic chemical shift values over the MD trajectory at 300 K does not improve the agreement (Fig. 8c).

18
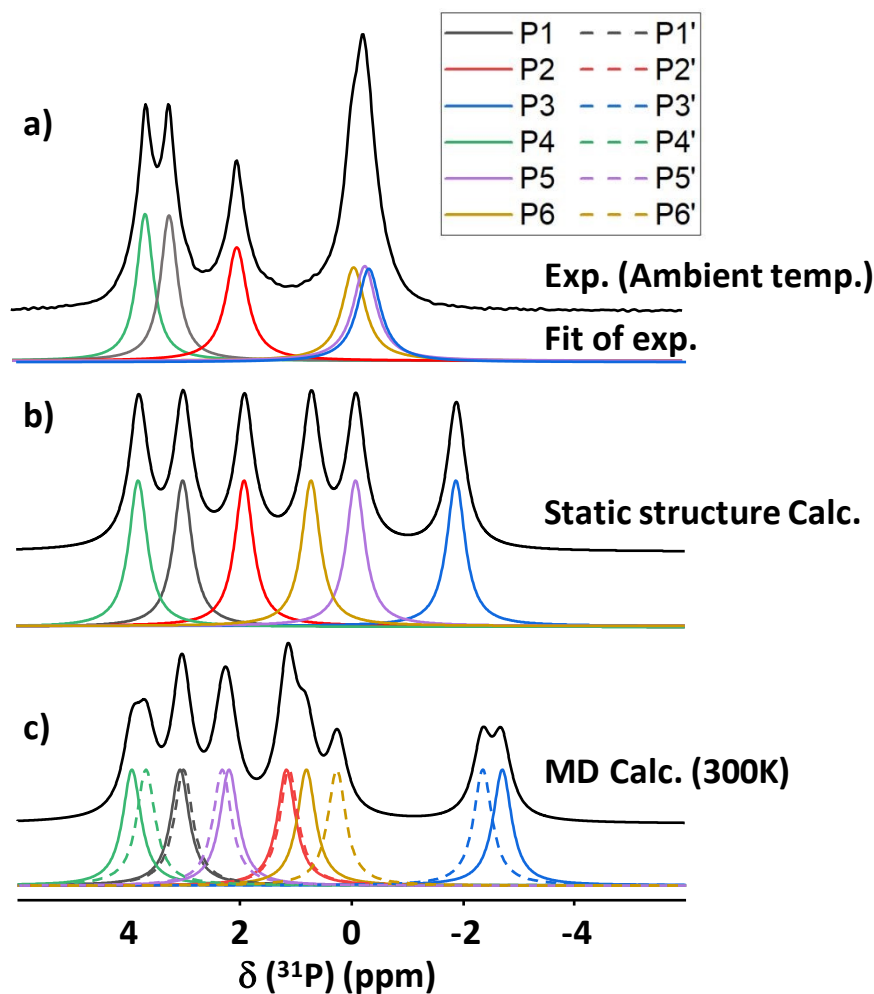
Figure 8: a) Experimental and fitted ^{31}P MAS NMR spectrum of OCP at "ambient temperature" (refrigerating unit set to 0°C), with resonances assigned according to Davies et al;[15] b) DFT-calculated ^{31}P chemical shifts for the relaxed static structure extrapolated at 298 K;[15]c) Time-averaged calculated ^{31}P chemical shifts after MD simulation at 300 K.

This discrepancy could be due to a variety of factors, such as an incorrectly sized crystal lattice, the presence of partially occupied sites, small changes in the water content in the interlayer space, and/or dynamics effects on time scales not explored by MD simulations. However, because of the significant computational cost of the MD simulations, trying to improve chemical shift prediction by further increasing the size of the OCP model (to take into account defects), increasing the time range of the calculations, and/or further analyzing the effect of small changes in the temperature, is beyond the scope of this study.

The NMR parameters of the other nuclei (^{1}H, ^{17}O, ^{43}Ca) were also calculated by DFT, and averaged over the length of the MD simulations at 100 K and 300 K. The calculated ^{1}H NMR parameters showed only relatively small differences between MD-averaged values at 300 K and 100 K, with the maximum change being of 1.1 ppm (Tab. S5). The calculated ^{43}Ca NMR parameters (δ_{iso} and C_Q) for the MD-averaged structures similarly showed little variation between 100 K and 300 K (except for δ_{iso}(Ca1'), which varies by ca. 6 ppm) (Tab. S3). Regarding ^{17}O NMR, the largest difference between both temperatures was found for the calculated chemical shift values. Notably, O9 and O9' (from the PO*H

groups involving P5 and P5') show a clear evidence of splitting at 100 K, but not at 300 K (differences in chemical shift values $\Delta\delta_{iso}(^{17}O)_{O9-O9', 100 K}$ = 16.0 ppm; $\delta_{iso}(^{17}O)_{O9-O9', 300 K}$ = 3.1 ppm) (Tab. S6). This significantly broadens the PO*H signal range, a change we can also observe on the experimental ^{17}O NMR spectra (Fig. 3c). The experimental broadening is also probably due to the increase in C_Q at low temperature, as suggested by the MD simulations and NMR calculations, which show an increase of 0.4 MHz for $|C_Q|(O9')$ when lowering the temperature from 300 K to 100 K.

Tentative assignment of calcium and oxygen sites in the ambient-temperature structures

As previously mentioned, at 35.2 T, the ^{43}Ca MAS NMR spectrum is still not fully resolved (Fig. 2c). Yet, it can be reasonably fitted at multiple fields with eight consistent components (Fig. S5), from which experimental δ_{iso}, C_Q and η_Q parameters can be extracted for each site. The quadrupolar parameter P_Q, which is directly related to C_Q and η_Q, was also estimated from complementary multifield analyses (see see supporting information Table S3 and related plots).

In a previous study on OCP, a tentative assignment of some of the ^{43}Ca resonances had been proposed, by comparison of experimental data with DFT-calculated values for a "static" model of the structure.[16] Here, to see if we could go further in the assignment of these signals, experimental values were compared with the averaged parameters from the MD simulations at 300 K (Tab. S3 and Fig. S9). The signal with the highest δ_{iso} value (46.8 ppm experimentally) also shows the largest quadrupolar coupling constant (C_Q > 4 MHz experimentally), in line with the calculated values for Ca6 and Ca6', which also show the highest δ_{iso} and C_Q, thereby allowing the safe assignment of this resonance. For the assignment of the other sites, the isotropic chemical shifts δ_{iso} were considered, because δ_{iso} has been shown to be a better criterion than quadrupolar parameters to discriminate ^{43}Ca resonances.[51] In doing so, three of the remaining signals, with isotropic chemical shifts of 19.9, 13.6, and −8.2 ppm, can be assigned to Ca2, Ca7 and Ca8, respectively, based on the calculated values for these sites. Lastly, the 4 overlapping central ^{43}Ca resonances can be divided into 2 groups, with the following assignments (based on calculations): one with δ_{iso} values at ~−0.5 ppm (Ca1 and Ca4), and the other with δ_{iso} values ~3 ppm (Ca3 and Ca5). This MD-proposed assignment remains consistent with our previously reported $^{43}Ca\{^1H\}$ REDOR study of OCP.[16] To try to go even further in the assignments of the last 4 sites, calculated $\delta_{iso}(^{43}Ca)$ values for each site in the averaged structures over 100 K and 300 K MD simulations were plotted against the averaged corresponding Ca···O distance (with a cut-off of 2.9 Å, see Fig. S10), as already proposed in the literature.[51] However, no strong correlation could be established. Overall, at this stage, no more precise assignment of the Ca sites can be proposed. Nevertheless, it can be noticed that the averaged parameters from the MD simulations at 300 K allow a more precise assignment of Ca2 and Ca7 compared to the previous calculations we had reported on a static model of OCP,[16] in which some components were more superimposed (Fig. S9).

Concerning the ^{17}O NMR data, the assignment of P-O sites (ranging from 105 to 130 ppm on the 1D ^{17}O MAS NMR spectrum) is too complicated considering the lack of resolution even at very high field (Fig. 2b) and the large number (22) of expected components. The two very distinct signals at around 75 and 90 ppm corresponding to POH environments can be safely assigned to O9 and O15 sites respectively, by comparison with calculated values (Tab. S6). The significant difference between both chemical shift values is potentially related to the differences in H-bonding, with O9-H1···O16 and O15-H6···O2 distances of 1.6 and 1.4 Å respectively in the 300 K MD simulation. This is also consistent with the ^1H − ^{17}O D-RINEPT experiment (Fig. 9), showing a stronger correlation of the ^{17}O P-OH signals of

higher frequency with the ^{1}H peak at 13 ppm. The latter can be safely assigned to H6 according to calculations, and based on the shorter O15-<u>H6</u>···<u>O2</u> distance (Tab. S5, Fig. S12).

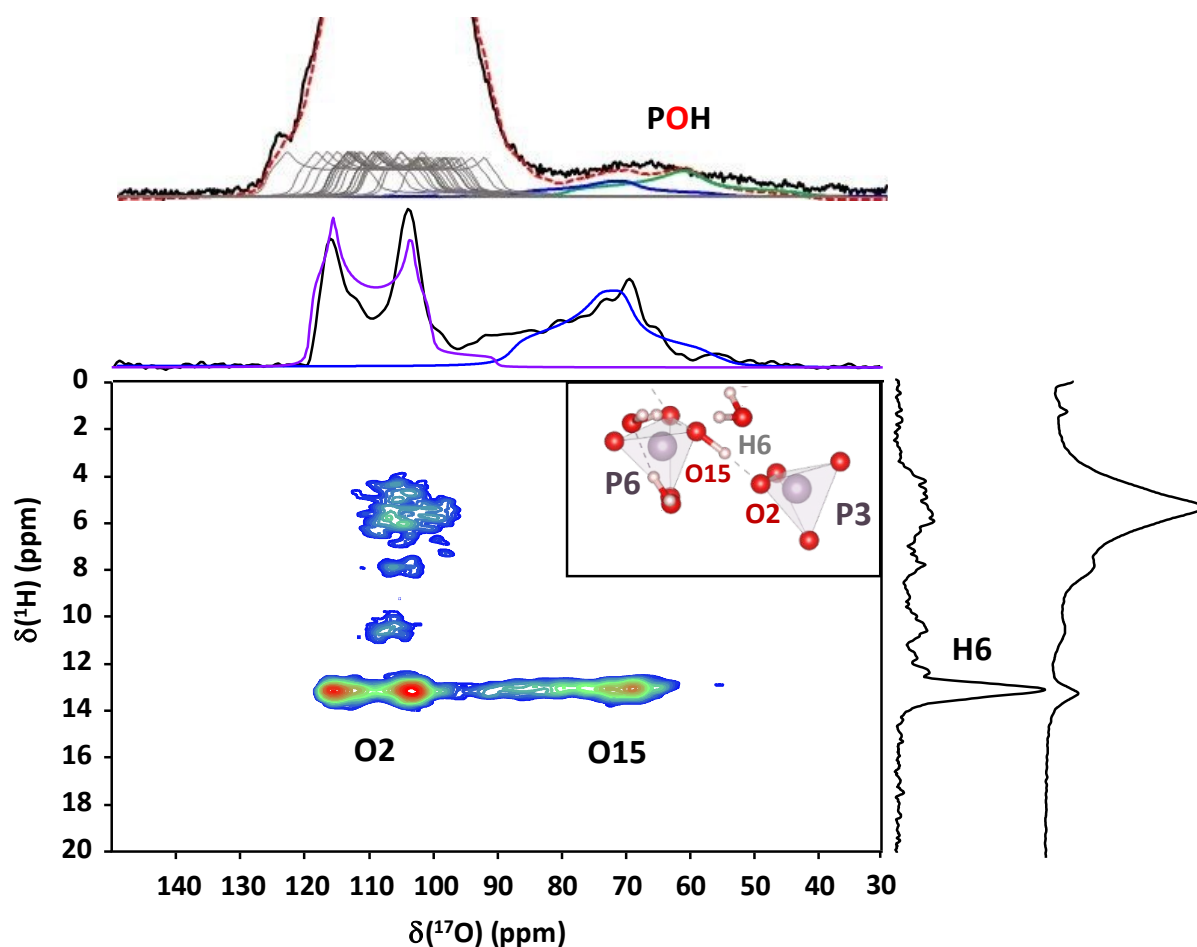*Figure 9: 2D heteronuclear ^{1}H-^{17}O D-RINEPT spectrum of the ^{17}O enriched OCP sample recorded at B_0 = 18.8 T and v_r = 50 kHz (refrigerating unit set to 5°C). Above the projections, the ^{1}H and ^{17}O direct acquisition NMR spectra are also presented in black. Regarding the ^{17}O projections, the direct excitation spectrum (top) was truncated to emphasize more the underlying individual components from PO (in grey) and POH groups (in blue and green), while the ^{17}O projection of the 2D data includes a fit of the H-bonded PO (O2, in purple) and POH (O15, in blue) sites.*

Surprisingly, only one clear cross-peak is observed for the POH groups in this D-RINEPT experiment. We would have expected two ^{17}O signals in the POH range, corresponding to O9 and O15 (respectively in green and blue on Figure 9). Yet, only O15 appears on the 2D, alongside the PO site that H6 is H-bonded to, which involves O2. This site was fitted to extract chemical shift (δ_{iso} = 121.9 ppm) and quadrupolar parameters (C_Q = 4.8 MHz and η_Q = 0.2). The latter were subsequently used, as a first approximation, for all the other PO sites of OCP, in the fit proposed on Figure 2b.

The lack of a cross peak for the other POH (involving O9) suggests that the dipolar recoupling between O9 and H1 must be significantly less efficient than that between O16 and H1, despite the similar distances in the static structure. This may be due to local motions around the POH, leading to an averaging of dipolar couplings and a faster relaxation. Indeed, rapid motions of water molecules

21

around O9 are observed on the MD at 300 K (Fig. S11), which are more pronounced than for O15. This raises the question about the position of the H1 signal. Indeed, Figure 2d shows that the ^{1}H signal at 13 ppm represents less than 7% of the overall signal, and therefore cannot correspond to both PO**H** peaks. According to calculations (Tab. S5 and Fig. S12), the H1 chemical shift position is expected between 8 and 10 ppm, due to a weaker O···H bond (distance around 1.6 Å). Unfortunately, because of the superimposition of the ^{31}P NMR resonances of P3, P5 and P6, the ^{1}H-^{31}P CP-HETCOR experiment recorded at room temperature did not allow the unambiguous determination of the ^{1}H chemical shift value of H1 (data not shown). However, it most likely sits at ca. 8 ppm: a ^{1}H peak at this position is clearly visible in the high-field ^{1}H NMR spectrum (Fig. 2d), which has a similar width and relative intensity as the peak at 13 ppm (H6 peak of the other PO**H**). Our later study of the 100 K structure will further confirm this assignment (vide infra), with a similar ^{1}H chemical shift for H1 at low temperatures observed both experimentally and on the GIPAW calculations of the MD structures at 100 K.

Tentative assignment of signals in the low-temperature structure

The assignment of peak positions of the different P sites at 100 K was then examined. From the quantitative direct excitation ^{31}P NMR experiments, it is possible to establish the following. Given a total integral for the signal of 12 a.u. (considering twelve resonances, as expected from the crystallographic structure in absence of symmetry), the rightmost peaks (from 1.0 to −2.0 ppm) integrate for 3.7 ± 0.3 a.u., the central peaks (from 2.5 to 1.0 ppm) integrate for 2.2 ± 0.2 a.u. and the leftmost peaks (from 4.5 to 2.5 ppm) integrate for 6.2 ± 0.2 a.u. leading to the fit presented on Figure 10a (with two peaks superimposed at 3.2 and 3.5 ppm, explaining their double intensity).
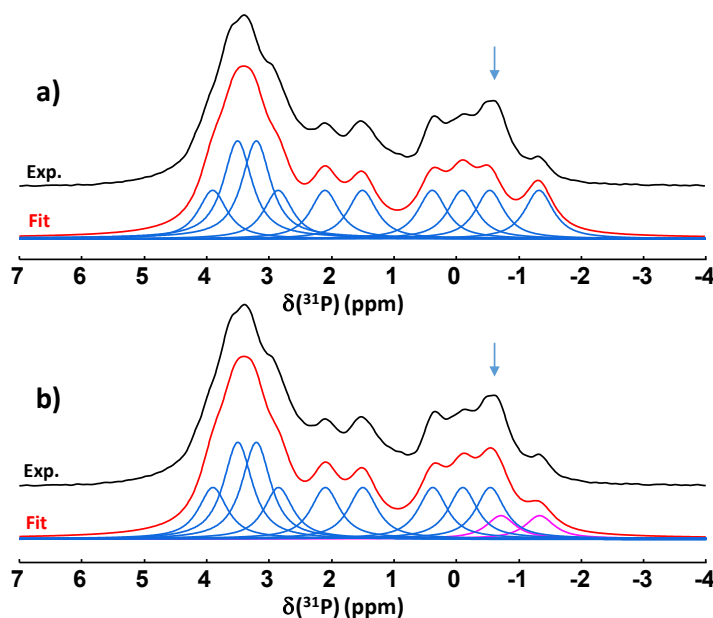

Figure 10 : Experimental ^{31}P MAS NMR spectrum of unenriched OCP sample at 100 K (B${}_0$ = 18.8 T and v${}_r$ = 8 kHz), and its fit (with Pseudo-Voigt peaks with a Gaussian/Lorentzian ratio of 0.4): a) attempts of fit with 12 sites of equal intensity (the resonances at 3.2 and 3.5 ppm have double intensity, due to the overlap of 2 sites at each of these positions), b) best fit, with the rightmost resonance split in two components of equal intensity (in pink) to match observed intensities. The blue arrow designates the area of the spectrum altered by the splitting of the resonance.

It is almost possible to fit the experimental signal using 12 Pseudo-Voigt peaks of equal intensity and width, distributed to match these integrations. However, to obtain a more suitable fit in the low frequency region, the rightmost resonance at −1.3 ppm must be reduced by half, and the missing intensity added as a new resonance at −0.7 ppm (see Fig. 10b, pink peaks; and Tab. S8 for fitting parameters). We will discuss the possible reasons for this splitting below.
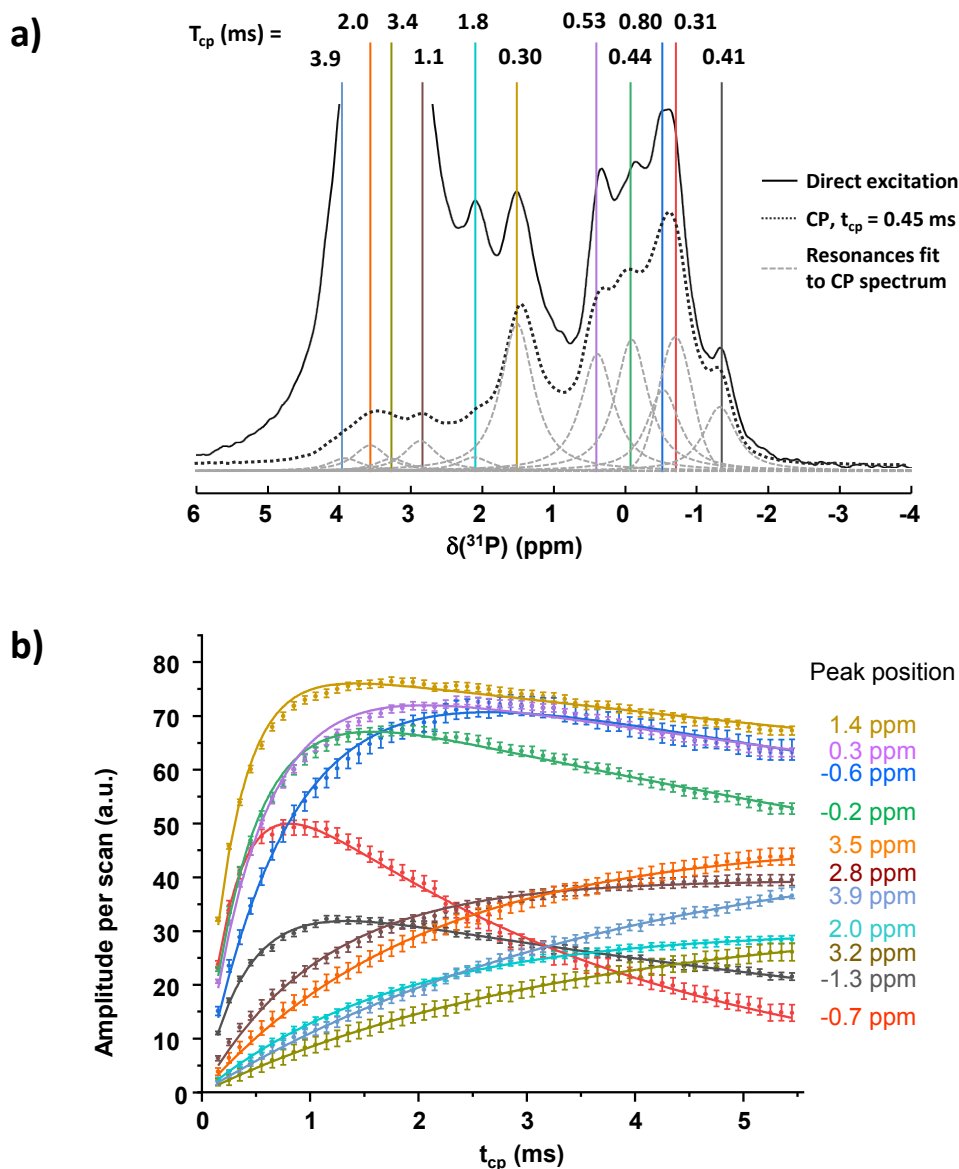

Figure 11: a) ^{31}P CPMAS spectrum (dotted black), recorded at ca. 100 K, using a contact time of 0.45 ms (B_0 = 18.8 T, ν_r = 8 kHz), in comparison to the direct-excitation ^{31}P NMR spectrum recorded at the same temperature (in black, voluntarily truncated vertically, to enable comparisons in the low-frequency region). The individual components (dashed light-grey) correspond to the resonances shown in Fig. 10b, with intensities adjusted to match the experimental CPMAS spectrum. Above the resonances are the CP time constants (T_{cp}) calculated for each individual resonance. b) Evolution of the amplitude of the different resonances of the ^{31}P CPMAS NMR spectra recorded on an unenriched OCP sample at ca. 100 K, at different contact times (t_{cp}). The curves correspond to a Levenberg-Marquardt regression of the data points using a simplified model for the transfer of polarisation from ^1H to ^{31}P (see experimental section for more details, and Table S9 for fitting parameters).

23

A first clue for the assignment of the sites at 100 K can be obtained by comparing the relative intensities in the direct-excitation ^{31}P MAS NMR spectrum to those in the ^{31}P CPMAS NMR spectra, which were recorded at various contact times (t_{cp}) Figure 11 shows that the sites with the slowest CP build-up are between 2.0 and 4.0 ppm, while the other sites show higher relative intensities at shorter contact times. Since sites corresponding to HPO_4^{2-} ions will have shorter build-up times, we can hypothesise that at least P5 and P6 sites (and their P5'and P6' counterparts) are among the lower chemical shift peaks (below 1.7 ppm), as is also the case at 300 K (Tab. S2).
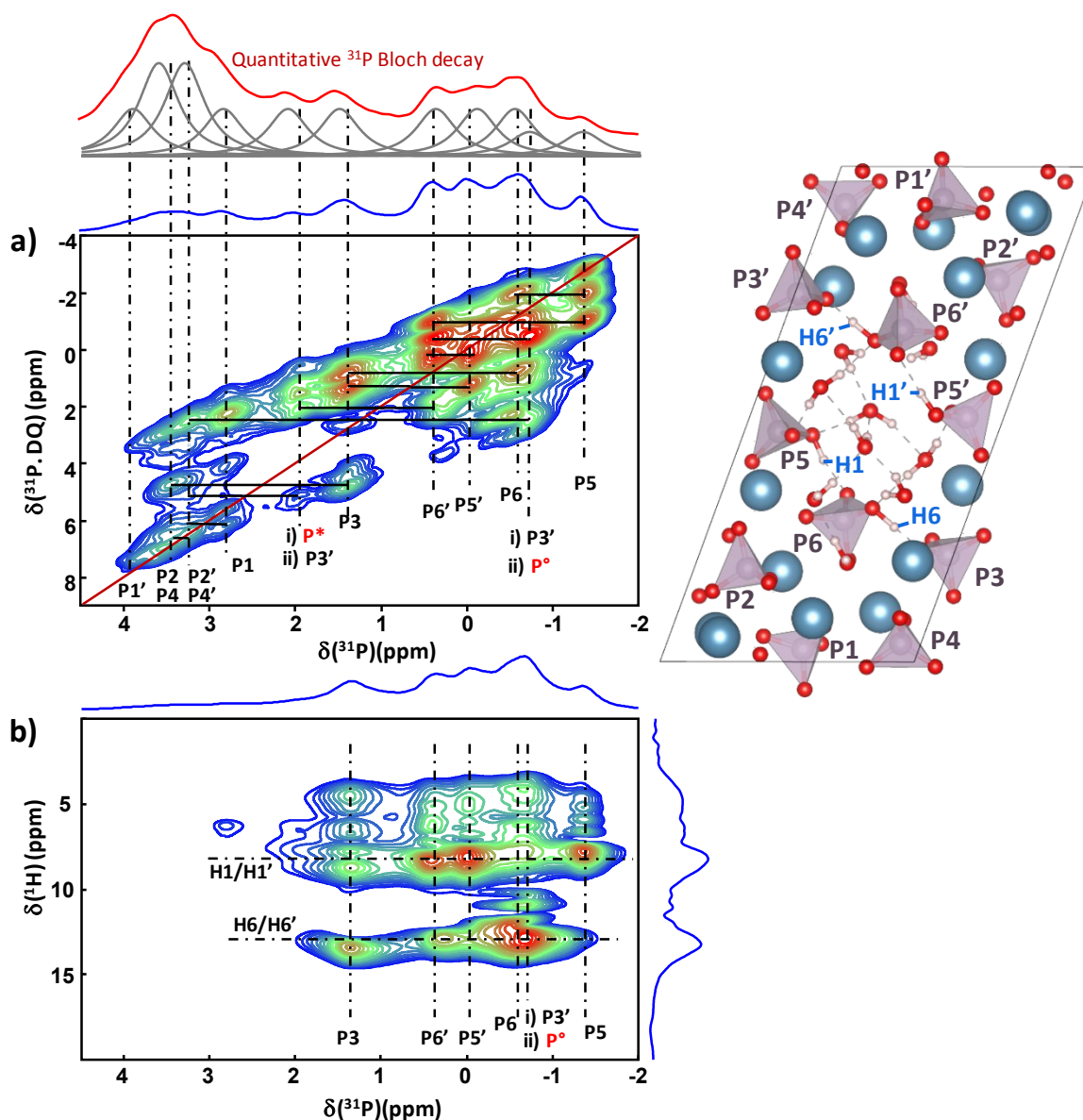

Figure 12: 2D NMR experiments recorded on unenriched OCP at ca. 100 K (temperature of the refrigerating unit): a) {^1H} ^{31}P -^{31}P DNP S3 DQ/SQ correlation spectrum recorded at 9.4 T, with a 7.4 ms recoupling time, and v_r = 13 kHz. The fit of the quantitative direct-excitation (Bloch decay) ^{31}P MAS NMR spectrum (recorded at 100 K) is shown in red above the figure. Small shifts in positions between DQ/SQ and direct-excitation MAS peaks are observed, possibly due to surface and/or DNP effects (as discussed in the manuscript). b) ^1H-^{31}P DNP CP-HETCOR spectrum recorded at 9.4 T; t_{cp} = 0.2 ms, v_r = 13 kHz. The symbols i) /ii) and P*/P° signal correspond to the 2 tentative assignments discussed in the main text.

Pair	Dist. (Å)	Pair	Dist. (Å)	Pair	Dist. (Å)	Pair	Dist. (Å)	Pair	Dist. (Å)	Pair	Dist. (Å)
P1 - P1'	4.09	**P2 - P3**	3.96	**P3 - P2**	3.96	**P4 - P4'**	4.02	**P5- P5'**	4.02	**P6 - P5**	4.09
P1 - P4'	4.73	**P2 - P4**	4.15	**P3 - P6**	4.15	**P4 - P2**	4.15	**P5 - P6**	4.09	**P6 - P3**	4.15
P1 - P2'	4.76	P2 - P1'	4.76	P3 - P4	5.10	P4 - P1'	4.73	P5 - P3	5.61	P6 - P2	5.08
P1 - P2	5.03	P2 - P1	5.03	P3 - P1	5.40	P4 - P1	5.03	P5 - P2'	5.88	P6 - P1	5.09
P1 - P6	5.09	P2 - P6	5.08	P3 - P4'	5.56	P4 - P3	5.10	P5 - P2	6.05	P6 - P3	5.75
P1 - P3	5.40	P2 - P5'	5.88	P3 - P5	5.61	P4 - P3'	5.57	P5 - P3'	6.65	P6 - P4	5.99
Pair	Dist. (Å)	Pair	Dist. (Å)	Pair	Dist. (Å)	Pair	Dist. (Å)	Pair	Dist. (Å)	Pair	Dist. (Å)
P1' - P1	4.09	**P2' - P3'**	3.98	**P3' - P2'**	3.98	**P4' - P4**	4.02	**P5'- P5**	4.02	**P6'- P5'**	4.06
P1' - P4	4.73	P2' - P4'	4.73	**P3' - P6'**	4.15	P4' - P1	4.73	**P5' - P6'**	4.06	**P6' - P3'**	4.15
P1' - P2	4.76	P2' - P1	4.76	P3' - P4'	5.10	P4' - P2'	4.73	P5' - P3'	5.64	P6' - P2'	5.08
P1' - P2'	5.00	P2' - P1'	5.00	P3' - P1'	5.41	P4' - P1'	5.02	P5' - P2	5.88	P6' - P1'	5.13
P1' - P4'	5.01	P2' - P6'	5.08	P3' - P4	5.57	P4' - P3'	5.10	P5 '- P3	5.88	P6' - P4'	6.02
P1' - P6'	5.13	P2' - P5	5.88	P3' - P5'	5.64	P4' - P1	5.54	P5 '- P2'	6.07	P6 '- P5	6.71

Table 1: **Interatomic distances between phosphorus sites in the averaged structure of OCP obtained by MD simulation at 100 K. Distances below 4.5 Å are highlighted in green.**

To try to further assist in the assignment, ^{31}P double quantum/single quantum (DQ-SQ) correlation spectra and ^{1}H-^{31}P CP-HETCOR experiments were recorded at 100 K, under DNP conditions (Fig. 12). Below, a tentative interpretation of these spectra is proposed. As a forenote, it should be noted that some of the cross-peaks on the DQ-SQ and HETCOR data are very slightly shifted compared to the peak-positions on the quantitative ^{31}P NMR spectrum. DQ-SQ analyses were performed using different recoupling times (Fig. S13), systematically showing similar features.

First, based on the CP build-up times (Fig. 11) and the P-H distances (Tab. S10), we expect the P1('), P2(') and P4(') ^{31}P signals to be positioned above 1.7 ppm, and P3('), P5(') and P6(') peaks below this value.

The ^{1}H-^{31}P CP-HETCOR experiment recorded using a short contact time of 0.2 ms (Fig. 12b) shows two main proton positions at ~ 8 ppm and ~ 13 ppm, that can be safely assigned to HPO$_4^{2-}$ resonances, based on the short P…H distances (Table S10). More precisely, they should correspond to H1/H1' and H6/H6', respectively, according to NMR calculations (Tab. S5). This is also consistent with the relative P5-O9-H1···O16-P6 and P6-O15-H6···O2-P3 distances, showing that there is a stronger H-bond in the latter case.[49] Consequently, P5(') and to a lesser extent P6(') sites are expected to show a cross-peak at ~ 8 ppm. Similarly, P6(') and P3(') sites should show a cross-peak at ~ 13 ppm. This means that the ^{31}P signals observed at 0.3, −0.2 and −1.3 ppm can correspond to P5(') and P6(') sites, while those at 1.4, 0.3, −0.6, −0.7 could belong to P6(') and P3(') sites.

The DQ-SQ experiment shown on Fig. 12a was measured with a 2 ms CP polarisation transfer from ^{1}H, and a recoupling time of 7.4 ms. Considering only the shortest calculated ^{31}P-^{31}P interatomic distances (below 4.5 Å), 10 main cross-peaks are expected (Tab. 1), which we will focus on. P6 is supposed to have significant cross-peaks with P3 and P5. Therefore, we can propose that the signal at −0.6 ppm belongs to P6, that shows cross-peaks with the signals at 1.4 and −1.3 ppm, that could thus belong to P3 and P5. Moreover, since P2, expected above 1.7 ppm, is close to P3, it could correspond to the peak at 3.5 ppm, showing cross-peak with the signal at 1.4 ppm. Note that two superimposed signals are suggested at 3.5 ppm by the quantitative ^{31}P NMR spectrum (Fig. 10), and that a cross-peak is

Faraday Discussions Accepted Manuscript

observed on the diagonal at 3.5 ppm. This suggests that P4, in close proximity to P2, may also observed at 3.5 ppm.

At this stage, we propose two possibilities for the Px(') assignments, both of which still present residual inconsistencies with the collected experimental data. Moreover, it should be noted that the ^{31}P calculated values after averaging by MD at 100 K show unfortunately too many discrepancies with experimental data, making their use for spectral assignments impossible at this stage.

i) A first possibility is to assign the signal at –0.7 ppm to P3', based on the ^{1}H-^{31}P CP HETCOR analysis. Since this signal shows cross-peaks with ^{31}P signals at 3.2 and 0.3 ppm on the DQ-SQ spectrum, the latter would be assigned to P2' and P6', respectively. The remaining signal visible on the CP-HETCOR experiment at –0.2 ppm, showing a cross-peak with the signal at 0.3 ppm (P6') would then correspond to P5'. Finally, the signal at 3.2 ppm showing a cross-peak with the signal at –0.7 ppm (P3') could be assigned to P2', superimposed with P4' (as previously proposed for P2/P4). The ^{31}P signal at 2.8 ppm showing cross-peaks with P4' and P2' (both at 3.2 ppm) is tentatively assigned to P1. P1 should show a cross-peak with P1', but no clear correlation is observed with the remaining signals. Here, it is proposed that the very low intensity peak at 3.9 ppm corresponds to P1' (its low intensity possibly preventing the observation of a cross-peak on the DQ-SQ experiment). A remaining ^{31}P NMR signal centered at 2.0 ppm (noted P*) is observed. It is likely to be part of the OCP phase as well, as it shows small cross-peaks with other OCP signals. Yet its assignment is uncertain. Moreover, in all this reasoning, the relative intensities of the ^{31}P resonances observed in the quantitative analysis (Fig. 10b) are not explained here.

ii) A second possibility is to take into account the fact that the intensity of the signal assigned to P5 (-1.3 ppm) is half of the others according to the quantitative spectrum (pink resonance on Fig 10b). This could suggest that the other half-intensity peak (at –0.7 ppm) is a P5-like site (noted P°), but with a different H-bonding for the POH since it shows cross-peaks with proton signals at ∼ 13 ppm and ∼ 10 ppm on the ^{1}H-^{31}P CP-HETCOR experiment. This implies that the remaining ^{31}P signals visible on the CP-HETCOR experiment at 0.3 and –0.2 ppm, showing a cross-peak on the DQ-SQ, would belong to P6' and P5' respectively. The small cross-peak between P6' (0.3 ppm) and the signal at 2.0 ppm on the DQ-SQ suggests the latter could be P3'. Finally, the signal at 3.2 ppm showing a cross-peak with the signal at 2.0 ppm (P3') could be assigned to P2', superimposed with P4' (as previously explained for P2/P4). By elimination and consistently with hypothesis *i)*, remaining signals at 3.9 and 2.8 ppm would possibly correspond to P1' and P1. However, in this second tentative assignment, P3' would not be visible on the ^{1}H-^{31}P CP-HETCOR data, and would also show slower ^{1}H-^{31}P CP dynamics, for unexplained reasons.

In both interpretations presented above, there are still common inconsistencies, like the unexpected presence of an on-diagonal cross-peak for P5, the absence of the expected cross-peak between P5 and P5', and the unexpected cross-peaks observed between P3 and P6, but also between P5 and P6'. In addition, P* and P° assignments are difficult to confirm at this stage, and in hypothesis *ii)*, P3' would also have a very different ^{1}H-^{31}P CP dynamics than P3, for which we have no explanation.

Our reasoning above was based on the implicit hypotheses that OCP samples at ca. 100 K are perfectly stoichiometric, crystalline, with 110 well-defined and fully occupied atomic sites. The presence of unexpected cross-peaks indicates that there could be significantly more than 12 P sites, possibly due to an even smaller symmetry (at least in some crystals, and/or some unit cells). Moreover, surface

effects may have an influence on the observations made by ssNMR. Indeed, even well-crystallised OCP platelets have a thickness of only a few unit cells (< 15 nm),[52] and the samples studied here also show a dispersion in the size of the particles (Fig. S3). Thus, the importance of the surface, particularly under DNP analysis conditions, may cause the observations made by NMR to partly diverge from those of an "ideal" model of OCP (which is built on experimental observations initially made on large single-crystals). These surface effects may not be apparent at ambient temperature, but the increased resolution and surface sensitivity of low-temperature DNP-enhanced experiments may have revealed (hydrogen)phosphate local environments that are not resolved under more standard analytical conditions. Simulating the surface of OCP separately from the bulk may be of interest in the case of OCP, although this is beyond the scope of our present study.

Lastly, regarding ^{17}O NMR data, a ^{1}H-^{17}O D-HMQC correlation experiment was performed at 100 K (Fig. 13). Here, contrary to the ^{1}H – ^{17}O correlation D-RINEPT experiment recorded at ambient temperature (Fig. 9), two cross-peaks are now visible, correlating the ^{1}H positions around 13 and 8 ppm with the ^{17}O resonances in the POH region, with isotropic shifts around ca. 90 and 75 ppm respectively. According to calculations (Tab. S5 and S6) and to the assignments proposed at ambient temperature, these cross-peaks correspond to the H6/H6' (13 ppm) - O15/O15' (90 ppm) and H1/H1' (8.5 ppm) - O9/O9' (75 ppm) pairs, respectively. This suggests that at low temperature, motions around O9 and H1 are reduced, enabling a cross-peak to be observed the ^{1}H-^{17}O dipolar-recoupling experiment. This is confirmed by comparing the results of MD simulations around this site at 100 K and 300 K (Fig S11). This assignment is also consistent with ^{1}H-^{31}P HETCOR results, since the P6/P6' sites are linked to O15/O15', and show a cross-peak with H6/H6' at ~ 13 ppm, while the P5/P5' sites are linked to O9/O9' and show a cross-peak with H1/H1' at ~ 8 ppm (Fig. 12b). At this stage, no further information about the low-temperature form of OCP could be extracted from this ^{17}O NMR data.
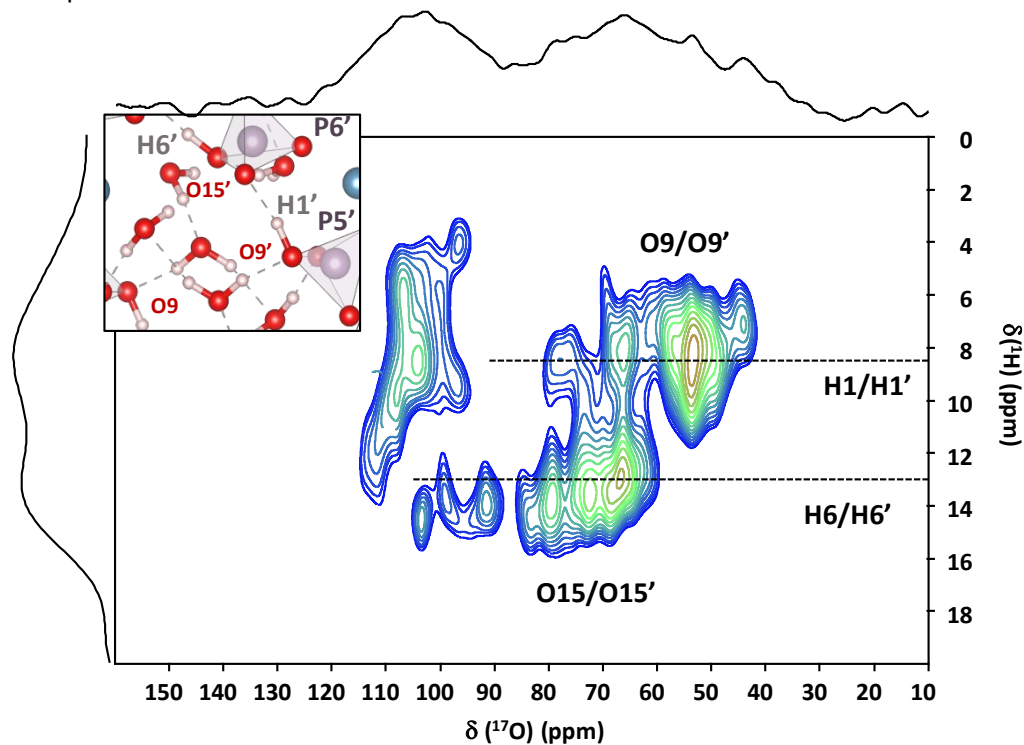

Figure 13: 2D heteronuclear ^{1}H-^{17}O D-HMQC spectrum of the ^{17}O-enriched OCP sample recorded at ca. 100 K (temperature of the refrigerating unit), B_0 = 18.8 T and v_r = 50 kHz.

Conclusion

We have demonstrated using solid-state NMR that OCP exhibits a significant mobility of water in the interlayer space, which is drastically reduced when cooled down at cryogenic temperatures. Using an "NMR crystallography" approach, involving variable-temperature ssNMR analyses, molecular dynamics simulations, and GIPAW-DFT calculations of NMR parameters, we propose that the OCP lattice can be found in different symmetry groups: $P1$ when observed at short timeframes or at low temperature, but P-1 when averaged over longer times or at high temperature. The lowered symmetry is caused by the asymmetric formation of low-energy H-bonds between water molecules, that become unstable at higher temperatures, due to reorientions of water molecules at a very short time scale.

While the reduction in crystal symmetry appears very clearly on the ^{31}P ssNMR data recorded at 100 K, several aspects of the OCP structre are nevertheless still unexplained. Indeed, molecular dynamics simulations help justifying the observed splitting of ^{31}P NMR peaks below 200 K, allow a more precise assignment of some ^{43}Ca sites at ambient temperature, and also help rationalise the differences observed on the ^{1}H-^{17}O dipolar-based correlations at 100 and 300 K. Nonetheless, MD does not facilitate the rationalisation of the low-temperature ^{1}H-^{31}P CP-HETCOR and ^{31}P/^{31}P DQ/SQ NMR data, nor help improve the quality of the agreement with the GIPAW calculated ^{31}P NMR parameters of the phosphorous sites in OCP. For this nucleus, it could be that NMR parameters are very sensitive to numerous effects, including the presence of partially occupied sites, small changes in local symmetry, small changes in the water content in the interlayer space, and/or dynamics effects on time scales not explored by MD simulations. While additional information on water dynamics may be accessible from ^{2}H experiments,[50] the synthesis of ^{2}H-enriched OCP was not attempted as part of this contribution, as an overlap between 24 ^{2}H sites was expected, thereby requiring extensive complementary studies to ensure accurate interpretation.

All in all, the present work highlights the limitations in studying hydrated phases solely at ambient temperature and using static models, and the importance of low-temperature NMR and molecular dynamics simulations in such cases.[53] It also opens the possibility of studying the mechanism of transformation of OCP into HAp in even more detail, given the improved resolution afforded by low temperatures and new knowledge about the structure of OCP. It seems, however, that the periodic boundary conditions usually used to analyse such structures may be a limiting factor in further computational studies of this phase. The use of more "costly" computational approaches, involving supercells and surface simulations, will probably be necessary for a deeper understanding of the OCP structure.

Author Contributions

The project was conducted by AN, in close interaction with DL and CG. AN carried out the syntheses and isotopic enrichment experiments, background characterisations, as well as the vast majority of ssNMR experiments. IH, AV and ZG performed the high-resolution ambient temperature experiments at 18.8 T and 35.2 T. SP and WP conducted and contributed to the analysis of the low-temperature ^{31}P NMR experiments recorded at 9.4 T. TF participated to the ambient temperature ^{43}Ca NMR experiments recorded at 23.4 T. DG participated to the low-temperature temperature ^{17}O NMR experiments recorded at 18.8 T. AN and CG carried out GIPAW DFT computations and MD calculations. AN, CG, DL, CB, GP, SH, WP and SP participated in discussions on ssNMR data of OCP. AN, CG and DL

wrote the initial draft of the manuscript, and all authors contributed to the final preparation of the article.

Conflicts of interest

In accordance with our policy on Conflicts of interest please ensure that a conflicts of interest statement is included in your manuscript here. Please note that this statement is required for all submitted manuscripts. If no conflicts exist, please state that "There are no conflicts to declare".

Acknowledgements

Faraday Discussions Accepted Manuscript

References

1 W. E. Brown, J. R. Lehr, J. P. Smith and A. W. Frazier, *J. Am. Chem. Soc.*, 1957, **79**, 5318–5319.

2 P. Simon, D. Grüner, H. Worch, W. Pompe, H. Lichte, T. El Khassawna, C. Heiss, S. Wenisch and R. Kniep, *Sci. Rep.*, 2018, **8**, 1–17.

3 M. Robin, S. Von Euw, G. Renaudin, S. Gomes, J. M. Krafft, N. Nassif, T. Azaïs and G. Costentin, *Cryst. Eng. Comm.*, 2020, **22**, 2728–2742.

4 G. R. Sauer, W. B. Zunic, J. R. Durig and R. E. Wuthier, *Calcif. Tissue Int.*, 1994, **54**, 414–420.

5 N. J. Crane, V. Popescu, M. D. Morris, P. Steenhuis and M. A. Ignelzi, *Bone*, 2006, **39**, 434–442.

6 E. Davies, K. H. Müller, W. C. Wong, C. J. Pickard, D. G. Reid, J. N. Skepper and M. J. Duer, *Proc. Natl. Acad. Sci.*, 2014, **111**, E1354–E1363.

7 R. Horváthová, L. Müller, A. Helebrant, P. Greil and F. A. Müller, *Mater. Sci. Eng. C*, 2008, **28**, 1414–1419.

8 W. E. Brown, *Nature*, 1962, **196**, 1048–1050.

9 C. Rey, C. Combes, C. Drouet and M. J. Glimcher, *Osteoporos. Int.*, 2009, **20**, 1013–1021.

10 Y. Wang, S. Von Euw, F. M. Fernandes, S. Cassaignon, M. Selmane, G. Laurent, G. Pehau-Arnaudet, C. Coelho, L. Bonhomme-Coury, M. M. Giraud-Guille, F. Babonneau, T. Azaïs and N. Nassif, *Nat. Mater.*, 2013, **12**, 1144–1153.

11 P. W. Arnold, *Trans. Faraday Soc.*, 1950, **46**, 1061–1072.

12 M. Mathew, W. E. Brown, L. W. Schroeder and B. Dickens, *J. Crystallogr. Spectrosc. Res.*, 1988, **18**, 235–250.

13 Y. H. Tseng, J. Zhan, K. S. K. Lin, C. Y. Mou and J. C. C. Chan, *Solid State Nucl. Magn. Reson.*, 2004, **26**, 99–104.

14 W. E. Brown, J. P. Smith, J. R. Lehr, and A. W. Frazier, *Nature*, 1962, **196**, 1050–1055.

15 E. Davies, M. J. Duer, S. E. Ashbrook and J. M. Griffin, *J. Am. Chem. Soc.*, 2012, **134**, 12508–12515.

16 D. Laurencin, Y. Li, M. J. Duer, D. Iuga, C. Gervais and C. Bonhomme, *Magn. Reson. Chem.*, 2021, **59**, 1048–1061.

17 F. Pourpoint, C. Gervais, L. Bonhomme-Coury, F. Mauri, B. Alonso and C. Bonhomme, *Comptes Rendus Chim.*, 2008, **11**, 398–406.

18 Z. Gan, I. Hung, X. Wang, J. Paulino, G. Wu, I. M. Litvak, P. L. Gor'kov, W. W. Brey, P. Lendi, J. L. Schiano, M. D. Bird, I. R. Dixon, J. Toth, G. S. Boebinger and T. A. Cross, *J. Magn. Reson.*, 2017, **284**, 125–136.

19 D. G. Cory and W. M. Ritchey, *J. Magn. Reson. 1969*, 1988, **80**, 128–132.

20 B. M. Fung, A. K. Khitrin and K. Ermolaev, *J. Magn. Reson.*, 2000, **142**, 97–101.

21 F. Mentink-Vigier, I. Marin-Montesinos, A. P. Jagtap, T. Halbritter, J. van Tol, S. Hediger, D. Lee, S. Th. Sigurdsson and G. De Paëpe, *J. Am. Chem. Soc.*, 2018, **140**, 11013–11019.

22 G. Teymoori, B. Pahari, B. Stevensson and M. Edén, *Chem. Phys. Lett.*, 2012, **547**, 103–109.

23 G. Teymoori, B. Pahari and M. Edén, *J. Magn. Reson.*, 2015, **261**, 205–220.

24 K. Märker, S. Paul, C. Fernández-de-Alba, D. Lee, J.-M. Mouesca, S. Hediger and G. D. Paëpe, *Chem. Sci.*, 2017, **8**, 974–987.

25 S. Paul, N. D. Kurur and P. K. Madhu, *J. Magn. Reson.*, 2010, **207**, 140–148.

26 C. Martineau, B. Bouchevreau, F. Taulelle, J. Trébosc, O. Lafon and J. P. Amoureux, *Phys. Chem. Chem. Phys.*, 2012, **14**, 7112–7119.

27 A. Brinkmann and A. P. M. Kentgens, *J. Am. Chem. Soc.*, 2006, **128**, 14758–14759.

28 A. P. M. Kentgens and R. Verhagen, *Chem. Phys. Lett.*, 1999, **300**, 435–443.

29 M. Goswami, P. J. M. Van Bentum and A. P. M. Kentgens, *J. Magn. Reson.*, 2012, **219**, 25–32.

30 J. J. Helmus and C. P. Jaroniec, *J. Biomol. NMR*, 2013, **55**, 355–367.

31 P. Virtanen, R. Gommers, T. E. Oliphant, M. Haberland, T. Reddy, D. Cournapeau, E. Burovski, P. Peterson, W. Weckesser, J. Bright, S. J. van der Walt, M. Brett, J. Wilson, K. J. Millman, N. Mayorov, A. R. J. Nelson, E. Jones, R. Kern, E. Larson, C. J. Carey, İ. Polat, Y. Feng, E. W. Moore, J. VanderPlas, D. Laxalde, J. Perktold, R. Cimrman, I. Henriksen, E. A. Quintero, C. R. Harris, A. M. Archibald, A. H. Ribeiro, F. Pedregosa and P. van Mulbregt, *Nat. Methods*, 2020, **17**, 261–272.

32 W. Kolodziejski and J. Klinowski, *Chem. Rev.*, 2002, **102**, 613–628.

33 J. Vandevondele, M. Krack, F. Mohamed, M. Parrinello, T. Chassaing and J. Hutter, *Comput. Phys. Commun.*, 2005, **167**, 103–128.

34 S. Grimme, J. Antony, S. Ehrlich and H. Krieg, *J. Chem. Phys.*, 2010, **132**, 154104.

35 S. Goedecker, M. Teter and J. Hutter, *Phys. Rev. B - Condens. Matter Mater. Phys.*, 1996, **54**, 1703–1710.

36 J. VandeVondele and J. Hutter, *J. Chem. Phys.*, 2007, **127**, 114105.

37 S. Nosé, *J. Chem. Phys.*, 1984, **81**, 511–519.

38 P. Giannozzi, S. Baroni, N. Bonini, M. Calandra, R. Car, C. Cavazzoni, D. Ceresoli, G. L. Chiarotti, M. Cococcioni, I. Dabo, A. Dal Corso, S. De Gironcoli, S. Fabris, G. Fratesi, R. Gebauer, U. Gerstmann, C. Gougoussis, A. Kokalj, M. Lazzeri, L. Martin-Samos, N. Marzari, F. Mauri, R. Mazzarello, S. Paolini, A. Pasquarello, L. Paulatto, C. Sbraccia, S. Scandolo, G. Sclauzero, A. P. Seitsonen, A. Smogunov, P. Umari and R. M. Wentzcovitch, *J. Phys. Condens. Matter*, 2009, **21**, 395502.

39 J. P. Perdew, K. Burke and M. Ernzerhof, *Phys. Rev. Lett.*, 1996, **77**, 3865.

40 P. Pyykkö, *Mol. Phys.*, 2018, **116**, 1328–1338.

41 B. K. Sahoo, *Phys. Rev. - At. Mol. Opt. Phys.*, 2009, **80**, 012515.

42 K. M. N. Burgess, Y. Xu, M. C. Leclerc and D. L. Bryce, *Inorg. Chem.*, 2014, **53**, 552–561.

43 C. R. Harris, K. J. Millman, S. J. van der Walt, R. Gommers, P. Virtanen, D. Cournapeau, E. Wieser, J. Taylor, S. Berg, N. J. Smith, R. Kern, M. Picus, S. Hoyer, M. H. van Kerkwijk, M. Brett, A. Haldane, J. F. del Río, M. Wiebe, P. Peterson, P. Gérard-Marchant, K. Sheppard, T. Reddy, W. Weckesser, H. Abbasi, C. Gohlke and T. E. Oliphant, *Nature*, 2020, **585**, 357–362.

44 I. Goldberga, I. Hung, V. Sarou-Kanian, C. Gervais, Z. Gan, J. Novák-Špačková, T.-X. Métro, C. Leroy, D. Berthomieu, A. van der Lee, C. Bonhomme and D. Laurencin, *Inorg. Chem.,* 2024*, accepted* (doi:10.1021/acs.inorgchem.4c00300).

45 M. Profeta, M. Benoit, F. Mauri and C. J. Pickard, *J. Am. Chem. Soc.*, 2004, **126**, 12628–12635.

46 G. Wu, D. Rovnyak, P. C. Huang and R. G. Griffin, *Chem. Phys. Lett.*, 1997, **277**, 79–83.

47 F. Pourpoint, C. Gervais, L. Bonhomme-Coury, T. Azaïs, C. Coelho, F. Mauri, B. Alonso, F. Babonneau and C. Bonhomme, *Appl. Magn. Reson.*, 2007, **32**, 435–457.

48 S. E. Ashbrook and M. E. Smith, *Chem. Soc. Rev.*, 2006, **35**, 718–735.

49 C. Gervais, C. Coelho, T. Azaïs, J. Maquet, G. Laurent, F. Pourpoint, C. Bonhomme, P. Florian, B. Alonso, G. Guerrero, P. H. Mutin and F. Mauri, *J. Magn. Reson.*, 2007, **187**, 131–140.

50 C. H. Chen, I. Goldberga, P. Gaveau, S. Mittelette, J. Špačková, C. Mullen, I. Petit, T. X. Métro, B. Alonso, C. Gervais and D. Laurencin, *Magn. Reson. Chem.*, 2021, **59**, 975–990.

51 D. Laurencin and M. E. Smith, *Prog. Nucl. Magn. Reson. Spectrosc.*, 2013, **68**, 1–40.

52 M. Iijima, H. Tohda and Y. Moriwaki, *J. Cryst. Growth*, 1992, **116**, 319–326.

53 I. Goldberga, N. D. Jensen, C. Combes, F. Mentink-Vigier, X. Wang, I. Hung, Z. Gan, J. Trébosc, T.-X. Métro, C. Bonhomme, C. Gervais and D. Laurencin, *Faraday Discuss.*, 2023, **241**, 250–265.

Faraday Discussions Accepted Manuscript